Contributions to Mineralogy and Petrology (2019) 174:15
https://doi.org/10.1007/s00410-019-1551-0

ORIGINAL PAPER

A refined model for lithosphere evolution beneath the decratonized northeastern North China Craton

A-Bing Lin[1] · Jian-Ping Zheng[1] · Qing Xiong[1] · Sonja Aulbach[2] · Jiang-Gu Lu[3] · Shao-Kui Pan[1] · Hong-Kun Dai[1] · Hui Zhang[1]

Received: 8 October 2018 / Accepted: 28 January 2019 / Published online: 5 February 2019

Abstract

The eastern North China Craton (NCC), where an initially diamondiferous deep cratonic mantle root was lost during Paleozoic and Mesozoic time, represents a prime natural laboratory to study the processes and mechanisms of continental lithospheric mantle destruction and replacement, which remain, however, controversial. In this study, detailed petrography, whole-rock and mineral compositions of spinel-facies peridotite xenoliths from Cenozoic basalts in the Huinan area, northeastern NCC, are presented to provide new constraints on the transformation of the subcontinental lithospheric mantle (SCLM). These xenoliths define two groups based on textural observation and mineral modes: Group 1 peridotites show protogranular textures and consist of harzburgites and dunites. They have low Al_2O_3 contents in whole-rock and orthopyroxene (0.53–1.06 wt.% and 2.10–3.21 wt.%, respectively), high olivine modes (79–96%), whole-rock MgO (44.8–47.9 wt.%) and Mg# (100 Mg/(Mg + Fe^T) molar: 90.1–90.7), suggesting that they were derived from moderately refractory SCLM. In contrast, Group 2 xenoliths display porphyroclastic to protogranular textures and consist of lherzolites and harzburgites with rare spinel-pyroxene intergrowths. They have overall higher Al_2O_3 (1.48–3.23 wt.% and 3.02–4.65 wt.%, respectively) in whole-rock and orthopyroxene, lower olivine modes (64–83%), MgO (38.6–44.5 wt.%) and whole-rock Mg# values 87.6–90.1, and they may represent fertile SCLM. Peridotites of both groups have similar equilibration temperatures (i.e., 923–977 °C and 881–1110 °C, respectively), which are not correlated with Mg# in olivines, suggesting that they coexist over a range of depths. However, clinopyroxenes in the Group 1 xenoliths display LREE-enriched and convex-upward REE patterns, whereas those in Group 2 mainly show LREE-depleted and spoon-shaped REE patterns, with minor LREE-enriched and convex-upward ones. In addition, spinel-pyroxene intergrowths indicative of garnet destabilization are ubiquitous in Group 1, consistent with variable Al_2O_3 over a narrow range of Mg# in some opx and low HREE in some cpx, but rare in Group 2 peridotites. Interaction of the fertile mantle with melts similar to the Cenozoic basalts at high melt–rock ratios eradicated most signatures of their origin in the garnet stability field, whereas the refractory peridotites, which reacted with residual melts or fluids at low melt/fluid-rock ratios, retained evidence for the former presence of garnet. We suggest that, combined, these observations are best reconciled if portions of ancient refractory lithosphere, which were partly delaminated during multiple subduction episodes affecting the eastern NCC, were re-accreted together with fertile mantle during asthenospheric upwelling driven by extension.

Keywords Peridotite xenoliths · Refertilization · Mantle metasomatism · Lithospheric mantle · North China Craton

Communicated by Timothy L. Grove.

Electronic supplementary material The online version of this article (https://doi.org/10.1007/s00410-019-1551-0) contains supplementary material, which is available to authorized users.

✉ Jian-Ping Zheng
jpzheng@cug.edu.cn

[1] School of Earth Sciences, State Key Laboratory of Geological Processes and Mineral Resources, China University of Geosciences, Wuhan 430074, China

[2] Goethe Universität, Institut für Geowissenschaften, Altenhöferallee 1, 60438 Frankfurt, Germany

[3] Key Laboratory of Submarine Geosciences, State Oceanic Administration, Second Institute of Oceanography, Ministry of Natural Resources, Hangzhou 310012, China

Introduction

The subcontinental lithospheric mantle (SCLM) plays a key role in the formation and evolution of continents over geological time (e.g., Griffin et al. 1998). In cratons, mantle roots are strongly depleted in basaltic components and have positive buoyancy and strong viscosity, which can make continents "float" on convective asthenosphere for billions of years (e.g., Frey and Green 1974; Walter 1998; Griffin et al. 1999a, b; O'Reilly et al. 2001; Bernstein et al. 2007; Lee et al. 2011; Tang et al. 2013). However, many studies show that the Archean cratonic lithospheric root could experience significant modification and even entire destruction (Foley 2008; Aulbach et al. 2017a). One well-studied example is the North China Craton (NCC) (e.g., Zheng 1999, 2009; Xu 2001; Gao et al. 2002; Zheng et al. 2007; Zhang et al. 2008; Dai et al. 2018). Mantle xenoliths and xenocrysts in Paleozoic diamondiferous kimberlites suggest that the NCC lithospheric mantle was Archean refractory mantle, which was thick (about 200 km) and cold (geotherms 36–40 mW/m^2) at least until the mid-Ordovician time (Zheng 1999). By contrast, xenoliths in Cenozoic basalts show the presence of fertile lithosphere, which was thin (< 90 km) and hot (50–105 mW/m^2) (Menzies et al. 1993; Zheng et al. 1998; Xu 2001; Gao et al. 2002; Zhang et al. 2008). These observations suggest great changes in the nature and thickness of the lithosphere (Gao et al. 2002; Zheng et al. 2007; Zhang et al. 2008). The mechanisms accounting for lithospheric modification have been proposed to be lithospheric delamination (Gao et al. 2004; Wu et al. 2005a) and/or asthenospheric erosion (Griffin et al. 1998; Zheng et al. 1998, 2007; Xu 2001), possibly along intra-lithospheric weak zones that are visible as mid-lithospheric discontinuities (MLD) in the neighboring intact cratonic mantle (Chen et al. 2014).

Mantle metasomatism can also cause severe chemical and mineralogical modifications in lithospheric mantle (e.g., Lee et al. 2011; O'Reilly and Griffin 2012; Tang et al. 2013; Xiong et al. 2015). Cryptic and modal types of metasomatism have been identified; the former refers to the mineral compositional alterations generated during infiltration of external fluids and/or melts (e.g., Ionov et al. 2002; Yu et al. 2005), while the latter would introduce newly crystallized minerals such as apatite, carbonates, amphibole and phlogopite (e.g., Rudnick et al. 1993; O'Reilly and Griffin 2012). The addition (and removal) of minerals that form part of the pre-existing assemblage has been termed "stealth metasomatism" and is, as the name implies, not straightforward to recognize based on mineralogy alone (O'Reilly and Griffin 2012). Identified metasomatic agents include aqueous fluids (Gorring and Kay 2000; Xu et al. 2003a), silicate melts (Zangana et al. 1999) and carbonatitic melts (Ionov et al. 1993; Rudnick et al. 1993). It is worth noting that the migration of the same fluids/melts within different domains or levels of lithospheric mantle would also form diverse metasomatic effects that could be mistaken as multiple episodes of metasomatism involving different types of fluids or melts (e.g., Navon and Stolper 1987; Vernières et al. 1997; Ionov et al. 2002; Yu et al. 2005).

The area of the northeastern NCC witnessed a complex evolution, including the closure of the Paleo-Asian Ocean from the north (Xiao et al. 2003) and subsequent subduction of the Paleo-Pacific Plate from the east (Tang et al. 2012; Zheng and Dai 2018). However, the specifics of the modification processes of the lithospheric mantle beneath this area, which resulted from its complex tectonothermal evolution, remain poorly constrained. In this contribution, we present detailed petrographic, whole-rock and in situ mineral elemental compositions of spinel-facies peridotite xenoliths from the Huinan Quaternary basalts in the northeastern NCC. Our aims are to shed new light on the nature and evolution of the lithospheric mantle beneath the northeastern part of the craton. Our findings provide new insights into the regional lithospheric architecture and reveal the complex processes of the partial replacement of the ancient SCLM in the tectonic framework of the Mesozoic-Cenozoic NCC destruction.

Geological setting

The North China Craton, with an Archean nucleus, is bounded by the Northeast China (NE China) fold belts to the north and a Pacific convergent system to the east (Fig. 1a). The craton contains three tectonic zones, i.e., the Eastern Block, the Central Zone and the Western Block (Zhao et al. 2000, 2005). The amalgamation of the Eastern Block and Western Block along the Central Zone during the Paleoproterozoic (~ 1.85 Ga) marks the final cratonization of the NCC (Zhao et al. 2005). The Eastern Block is composed mainly of Archean TTG gneisses, granitoids, granitic gneisses and supracrustal rocks (Zhao et al. 2000; Zhai and Santosh 2011) and remained tectonothermally quiescent until the middle Ordovician (Zhang and Yang 2007). During the Late Mesozoic and Cenozoic, the Eastern Block experienced multiple subductions (Windley et al. 2010) and significant decratonization (Zhu et al. 2012), as manifested by ubiquitous magmatism (Zhang et al. 2014), vigorous crustal deformation (Wang et al. 2011), widespread metallogenesis (Sun et al. 2007) and modification of the nature and thickness of the SCLM (Zheng et al. 1998, 2007; Zheng 1999), whereas the Western Block remains relatively stable with little crustal deformation and magmatism (Zhang et al. 2014).

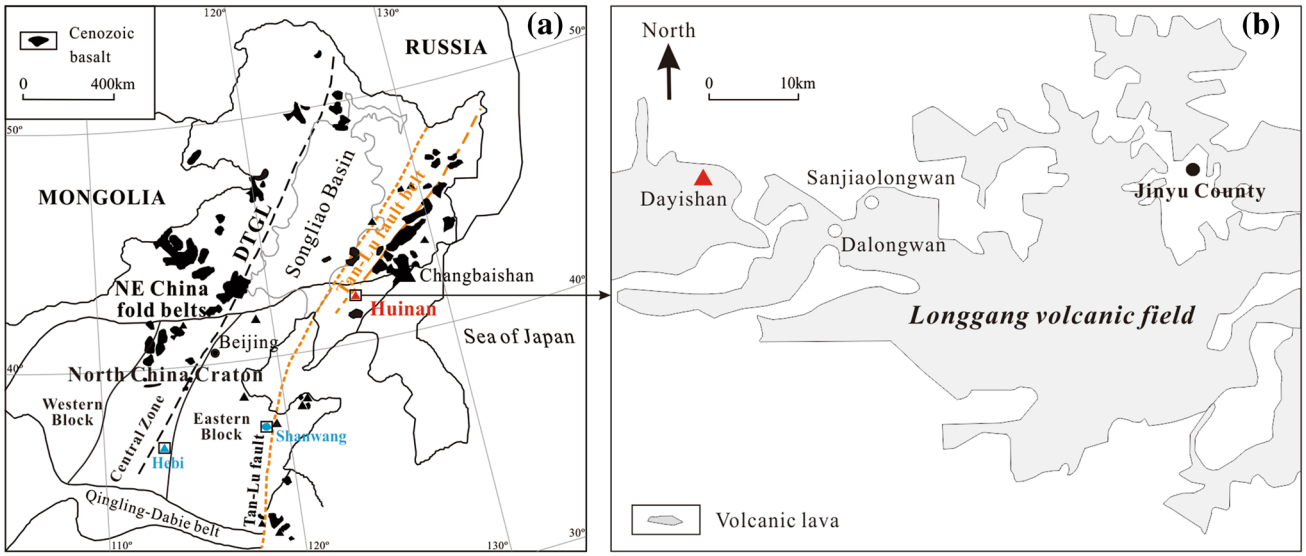

Fig. 1 Simplified tectonic units and distribution of Cenozoic basalts in North China Craton and Northeast China (NE China) fold belts (Fig. 1a) as well as the location of the Longgang volcanic field (Fig. 1b), revised after Xu et al. (2003b, 2012). The DTGL represents the Daxinganlin–Taihang gravity lineament

The Longgang volcanic field (LVF) in Jilin Province is located in the northeastern corner of the NCC, related to activation and development of the northern part of the Tan-Lu fault belt (T-L FB) (Fig. 1a; Liu et al. 1992). It covers an area of 1700 km^2 and consists of more than 160 Quaternary craters and calderas (Liu 1999), many of which were erupted in the early Pleistocene (0.6 Ma) (Fan et al. 2000). The eruption of LVF can be divided into three main periods, namely the Xiaoyishan Period (Early Pleistocene: 2.15–0.75 Ma), the Longgang Period (Middle-Late Pleistocene: 0.68–0.05 Ma) and the Jinglongdingzi Period (Holocene: 1600–1500 a.BP) (Fan et al. 2002). The basement of LVF consists dominantly of Archean metamorphic rocks. It is surrounded by a large number of basins that were developed in Cenozoic, the most famous of which is the Songliao Basin. These Cenozoic alkali basalts host abundant mantle-derived megacrysts and xenoliths, the latter mainly spinel-facies peridotites (Xu et al. 2003b; Wu et al. 2003; Lu and Zheng 2011; Tang et al. 2012). The studied Huinan peridotites are all collected from Dayishan (Fig. 1b).

Sample descriptions and petrography

The Huinan peridotites, part of the LVF, are very abundant and fresh with round to angular shapes and are about 1–20 cm in diameter. The studied samples are all spinel facies, including predominantly harzburgites, subordinately lherzolites and newly found dunites.

Peridotites of Group 1 have dominantly protogranular microstructures, high olivine modes of at least 84 vol.%, except one sample of 79 vol.%, and are composed of harzburgites and dunites (detailed mineral assemblage and modes can be found in Table S1). A few olivine and orthopyroxene grains exhibit kink bands and show curvilinear or irregular grain boundaries, with occasional 120° triple junctions. Spinel occurs as individual grains at the rims of large orthopyroxenes or as pyroxene–spinel clusters (intergrowths of orthopyroxene + spinel) that together mimic ovoid grain shapes (Fig. 2a, b). Exsolution lamellae and some fluid/melt inclusions are present in some large orthopyroxene porphyroclasts (Fig. 2c, d).

Group 2 peridotites show lower olivine modes (64–83 vol.%) but higher clinopyroxene modes (3–14 vol.%) compared with those of Group 1 (79–96 vol.% and < 1 vol.%, respectively) and consist of lherzolites and harzburgites with transitional textures between protogranular and porphyroclastic textures (Fig. 2e) or porphyroclastic textures (Fig. 2f). Orthopyroxene and clinopyroxene carry abundant exsolved spinel lamellae and fluid/melt inclusions (Fig. 2g). Kink bands, fractures and 120° triple junctions are common between olivine grains (Fig. 2h). Some orthopyroxenes are irregular in shape and partially enclose olivine. Spinel occurs as inclusions in olivines or as interstitial phases at grain boundaries. Rare pyroxene–spinel clusters are also observed in Group 2 peridotites.

Analytical methods

All analyses were performed in the State Key Laboratory of Geological Processes and Mineral Resources, China University of Geosciences (Wuhan). The major

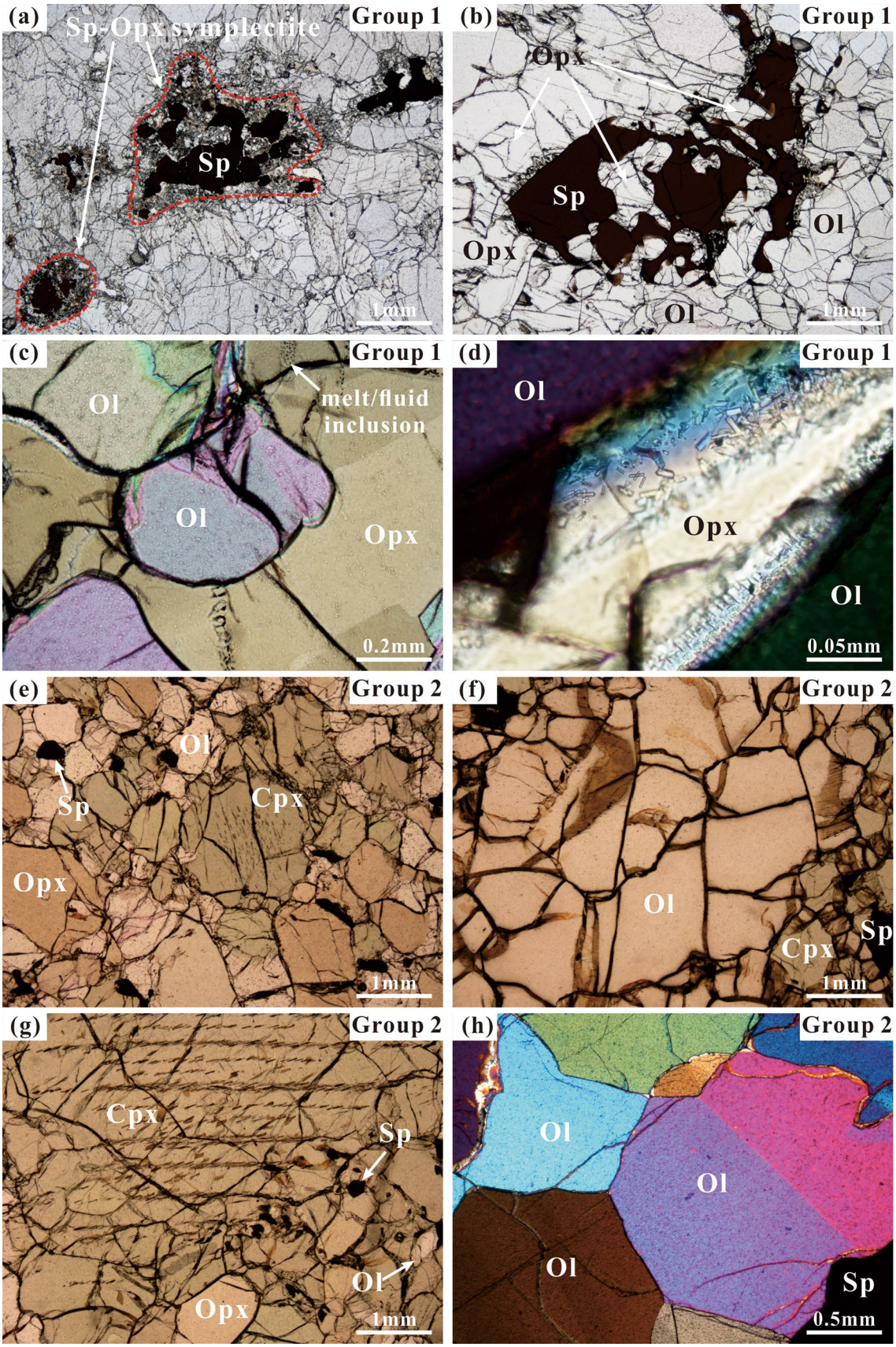
(a)
Group 1
Sp-Opx symplectite
Sp
1mm
(b)
Group 1
Opx
Sp
Ol
Opx
Ol
1mm
(c)
Group 1
Ol
melt/fluid inclusion
Ol
Opx
0.2mm
(d)
Group 1
Ol
Opx
Ol
0.05mm
(e)
Group 2
Ol
Sp
Cpx
Opx
1mm
(f)
Group 2
Ol
Cpx
Sp
1mm
(g)
Group 2
Cpx
Sp
Ol
Opx
1mm
(h)
Group 2
Ol
Ol
Ol
Sp
0.5mm

◂**Fig. 2** Petrographic features of the studied Huinan peridotite xenoliths. **a** Opx + sp symplectitic intergrowths in xenolith HNd-074. **b** Opx + Sp symplectite characterized by ovoid shape in xenolith HNd-075. **c** Olivine embayments partly corroding the orthopyroxene porphyroclast with melt/fluid inclusions in xenolith HNd-065. **d** The rims of opx in contact with olivine are riddled with tiny (~0.01 mm) minerals and melt/fluid inclusions in xenolith HNd-065. **e** Protogranular texture in xenolith HNd-083. **f** Porphyroclastic texture in xenolith HNd-090. **g** Cpx porphyroclast with exsolution lamellae in xenolith HNd-087. **h** 120° triple junctions between Ol grains in xenolith HNd-086. Photomicrographs for **a, c, d** and **h** are cross-polarized light. Plane-polarized light for **e, f** and **g**. *Ol* Olivine, *Opx* orthopyroxene, *Cpx* clinopyroxene, *Sp* spinel

element compositions of bulk rocks were measured by X-ray fluorescence (XRF) using fused glass disks, by fusion of 0.6 g of rock powder, 5 g of compound flux ($Li_2B_4O_7$:$LiBO_2$ = 12:22), 0.3 g NH_4NO_3 and 0.4 g LiF in a high-frequency furnace for 11 min at ~1050 °C in 95% Pt–5% Au crucibles. The melt was swirled repeatedly to ensure complete dissolution and homogenization of the material and then poured into a mould to form a thin flat-surfaced disc (34 mm diameter). The loss-on-ignition (LOI) was measured on dried rock powder by heating in a pre-heated corundum crucible to 1000 °C for 90 min and recording the percentage weight loss. XRF analysis was carried out on a Shimadzu XRF-1800 sequential X-ray fluorescence spectrometer, using an Rh-anode X-ray tube with a voltage of 40 kV and current of 70 mA. Calibration curves used for quantification were produced by bivariate regression of data from ~40 reference materials encompassing a wide range of silicate compositions. Analytical precision is better than 4% for major elements. The measurement procedure and data quality were monitored by repeated analyses (one between ten samples) of USGS standard BHVO-2 and Chinese National standards GBW07102. Results for reference materials are given in Table S2-RM, suggesting that the most element contents agree within 3% (analytical accuracy) with reference values.

In situ major-element compositions of minerals were determined by a JEOL JXA-8100 Electron Probe Micro-Analyzer (EPMA), equipped with four wavelength-dispersive spectrometers (WDS), using an accelerating voltage of 15 kV and a sample current of 20 nA. The nominal diameter of the electron beam was < 1 μm. Data were corrected online using a modified ZAF (atomic number, absorption, fluorescence) correction procedure. Element peaks and backgrounds were measured for all elements with counting times of 10 s and 5 s, respectively (except for Ti, Mn, these were 20 s and 10 s, respectively). The following standards were used for quantification: Jadeite (Na), Rutile (Ti), Pyrope Garnet (Al, Fe, Mg and Si), Rhodonite (Mn), Diopside (Ca) and Sanidine (K), Nickel (Ni).

In situ quantitative analyses of clinopyroxene for trace elements were conducted on thin sections using laser ablation–inductively coupled plasma–mass spectrometry (LA-ICP-MS) (GeoLas 2005 + Agilent 7500a) with an ablation spot size of 44 μm. Helium was used as a carrier gas and nitrogen was added into the central gas flow (Ar + He) of the Ar plasma to increase the sensitivity (Hu et al. 2008). Detailed operating conditions for the laser system and the ICP-MS instrument were described in Liu et al. (2008). Each analysis included approximately 20–30 s of background acquisition (from a gas blank) followed by 50 s of data acquisition from the sample. NIST SRM 610 was used to correct the time-dependent drift of sensitivity and mass discrimination. The element contents of samples, and of USGS reference glasses (BCR-2G, BHVO-2G and BIR-1G) measured as unknowns, were determined using the USGS reference glasses as reference materials for external calibration, without applying internal standardization, and normalization of the sum of all metal oxides to 100 wt.% was applied (Liu et al. 2008). Offline selection and integration of background and analytical signals, time-drift correction, and quantitative calibration were performed by ICPMSDataCal (Lin et al. 2016; Liu et al. 2008). Results for reference materials are given in Table S4-USGS, with most element concentrations agreeing within 10% or better with accepted values.

Results

Whole-rock compositions

Compared to the Group 2 xenoliths, Group 1 peridotites have lower Al_2O_3 contents (0.53–1.06 wt.% vs. 1.48–3.23 wt.%) and higher MgO (Figs. 3, 4). The contents of Al_2O_3, CaO and TiO_2 show negative correlations with MgO, and the concentrations of Al_2O_3 and CaO, but not FeO, are lower than those of commonly accepted primitive upper mantle compositions (Figs. 3, 4; e.g., McDonough and Sun 1995). These compositional variations are similar to those expected for residues of variable degrees of partial melting and have been observed in other worldwide mantle xenoliths suites (Frey and Green 1974; Takazawa et al. 2000). FeO^T contents in both the Group 1 and Group 2 peridotites, however, do not correlate with MgO (Fig. 3d), which is not consistent with variable extraction of basaltic melts. In addition, the Mg# values (i.e., 100 × Mg/(Mg + Fe), atomic number) vary from 87.6 to 90.7 (Table S2). Specifically, the Group 1 peridotites show higher Mg# (90.1–90.7) and have an affinity with the high-Mg# group peridotites from Hebi (suggested relics of refractory cratonic mantle; Zheng et al. 2001); Group 2 xenoliths display lower Mg# (87.6–90.1), which are similar to peridotite xenoliths from Shanwang (interpreted as newly accreted fertile lithosphere; Zheng et al. 1998) (Fig. 3).

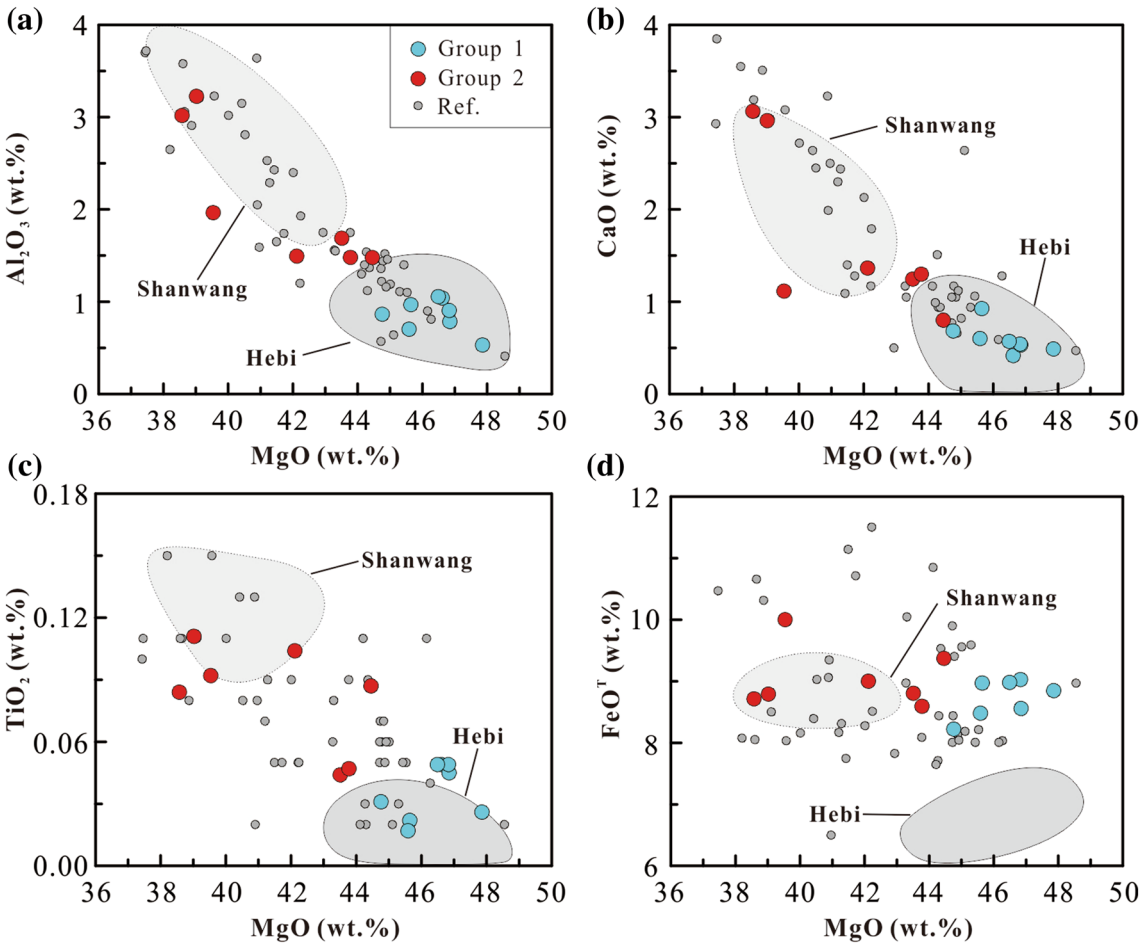

Fig. 3 Plots of **a** Al_2O_3, **b** CaO, **c** TiO_2 and **d** FeO^T as a function of MgO in whole-rock peridotite xenoliths from Huinan. Shown for comparison are field for peridotite xenoliths from Hebi and Shanwang. The Hebi peridotites are suggested to represent remnants of the Archean lithosphere preserved locally beneath the NCC (Zheng et al. 2001, 2007), whereas the mantle beneath Shanwang has been interpreted as newly accreted fertile material (Zheng et al. 1998). Ref. refers to the Huinan samples in previous studies (Xu et al. 1998, 2003b; Wu et al. 2003; Wang et al. 2013)

Major element compositions of minerals

Individual mineral grains (olivine, orthopyroxene, clinopyroxene and spinel) in these peridotites are commonly homogeneous by comparison of core and rim analyses by EPMA, except for spinel with sieve textures. Therefore, the average major-element compositions of minerals are used in this study (Table S3).

Olivines show a wide range in Mg# (88 to 91.5, mostly varying from 89.5 to 91.5). The highest Mg# (91.5) is found in sample HNd-68 (Group 1) and the lowest (88.0) in sample J297 (Group 2). Most olivines in Group 1 have higher Mg# than those in Group 2 (Table S3; Fig. 5a). There is a large range of TiO_2 contents in olivine of Group 2 (< 0.025–0.04 wt.%), but an apparently limited variation and lower contents in that of Group 1 (< 0.025 wt.%; Fig. 5a), although this observation must be considered in the context of most values being close to or below the detection limit.

Spinels in Group 1 peridotites have mostly higher contents of Cr_2O_3 (23.12–37.10 wt.% vs. 4.97–24.96 wt.%) and thus higher Cr# (26.3–44.3 vs. 5.2–28.7) than those of most samples in Group 2 (Table S3; Fig. 5b). Most samples in Group 1, with high Cr# and low Mg# in spinels, are different from the Group 2 peridotites displaying low Cr# but high Mg# in spinels (Fig. 5b). Meanwhile, the rims of sieve-textured spinels show higher Cr, Fe and Ti contents than those in the clear cores (Table S3).

Orthopyroxenes of Group 2 show large variations in Mg# (88.5–91.3), but limited range for that of Group 1 (91.3–92.1). Most opx in the Group 1 xenoliths have lower Al_2O_3 contents (2.10–3.21 wt.%) but higher Cr_2O_3 (0.43–0.48 wt.%) contents than those in the Group 2 xenoliths (3.02–4.65 wt.% and 0.17–0.60 wt.%, respectively) (Table S3; Fig. 5c, d).

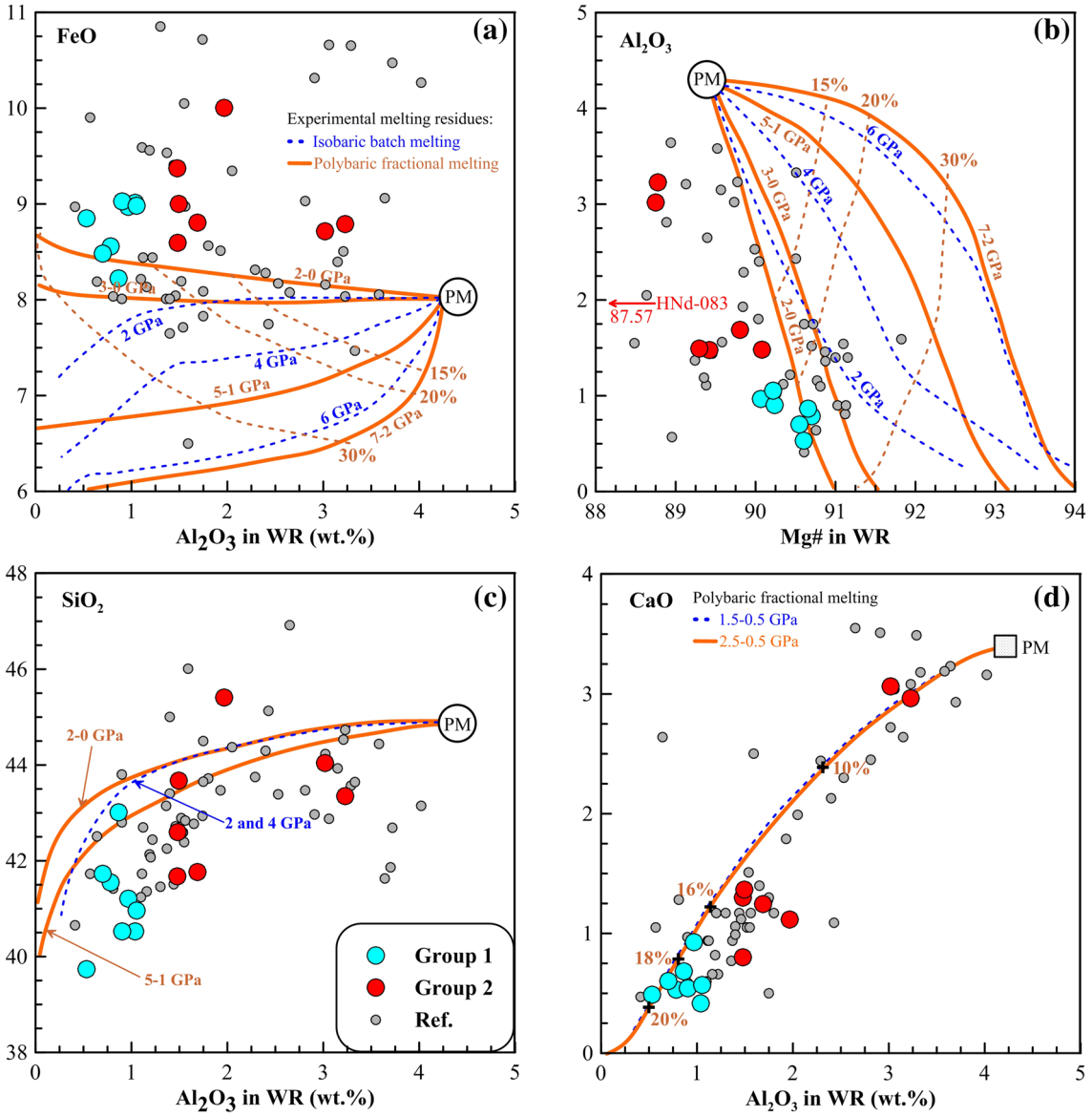

Fig. 4 Co-variation plots of whole-rock major oxides for peridotite xenoliths from Huinan. In Fig. 4a–c, dashed blue lines show isobaric batch melting residues formed at 2, 4 and 6 GPa; solid orange lines are residues of polybaric fractional melting at 2–0, 3–0, 5–1 and 7–2 GPa (Herzberg 2004); the dashed orange curves denote the contours of partial melting and the orange numbers (15%, 20%, and 30%) represent the degrees of melt extraction. In Fig. 4d, the dashed blue and solid orange curves represent the compositional trajectories for polybaric fractional melting at 1.5–0.5 GPa and at 2.5–0.5 GPa (Niu 1997), respectively; The orange numbers show the degrees of melt extraction at the black crosses. The compositions of primitive mantle (PM) are represented by the fertile peridotite KR4003 (Walter 1998) in Fig. 4a-c and the preferred source after Niu (1997) in Fig. 4d, respectively. Data sources are the same as those for Fig. 3

All clinopyroxenes analyzed here are Cr-diopside with 0.37–1.79 wt.% of Cr_2O_3. Compared to clinopyroxenes in the Group 2 xenoliths, clinopyroxenes in the Group 1 peridotites have higher Mg# (91.0-92.5) but lower Al_2O_3 (3.59–4.97 wt.%) contents and they display large ranges of TiO_2 and Na_2O contents (Fig. 5e, f). A sample (HNd-065) in Group 1 has the highest TiO_2 yet lowest Na_2O content (Table S3).

Trace-element compositions of clinopyroxene

Clinopyroxenes can be subdivided into four types, based on their REE patterns (Fig. 6): (1) Type 1 cpx are characterized by the lowest LREE/HREE values [$(La/Yb)_N = 0.08–0.78$], relatively flat HREE [$(Gd/Yb)_N = 0.72–1.67$] (Table S4; Fig. 6a), and obvious negative anomalies in Nb, Zr and Ti (Fig. 6b) and are prevalent in the lherzolites dominating in Group 2 xenoliths;

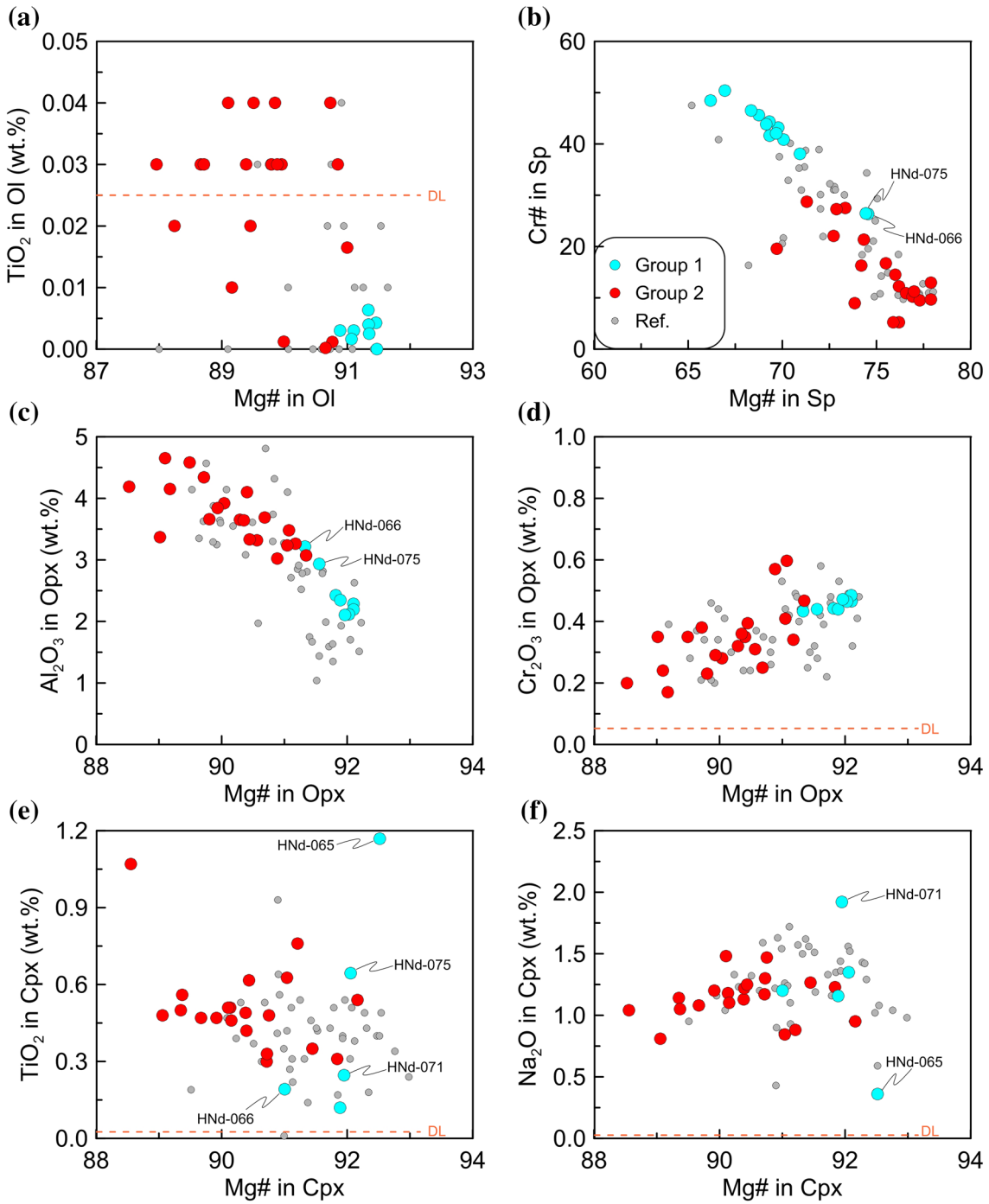

Fig. 5 Oxide concentrations or Cr# (100Cr/(Cr + Al) molar) in olivine, spinel, orthopyroxene and clinopyroxene from Huinan xenoliths as a function of Mg# (100 Mg/(Mg + Fe^T) molar). The orange dotted line in **a, d, e** and **f** denotes the average detection limit (DL). Data sources as in Fig. 3

(2) Type 2 cpx show spoon-shaped patterns (Fig. 6c) and negative anomalies in Nb, Zr and Ti (Fig. 6d) and occur in two samples of Group 2 lherzolites; (3) Type 3 cpx display the highest LREE/HREE values [$(La/Yb)_N = 6.23–8.37$], slightly HREE-depleted patterns [$(Gd/Yb)_N = 1.19–1.65$] (Table S4; Fig. 6e), and negative anomalies in Nb and Ti (Fig. 6f) and are found in HNd-066 (Group 1) and J298 (Group 2); and (4) Type 4 cpx show convex-upward patterns, high MREE/HREE, but lower LREE/MREE (Fig. 6g) and negative anomalies in Nb and Ti (Fig. 6h) and occur in Group 1 sample (HNd-071) and two Group 2 samples (J230 and J297).

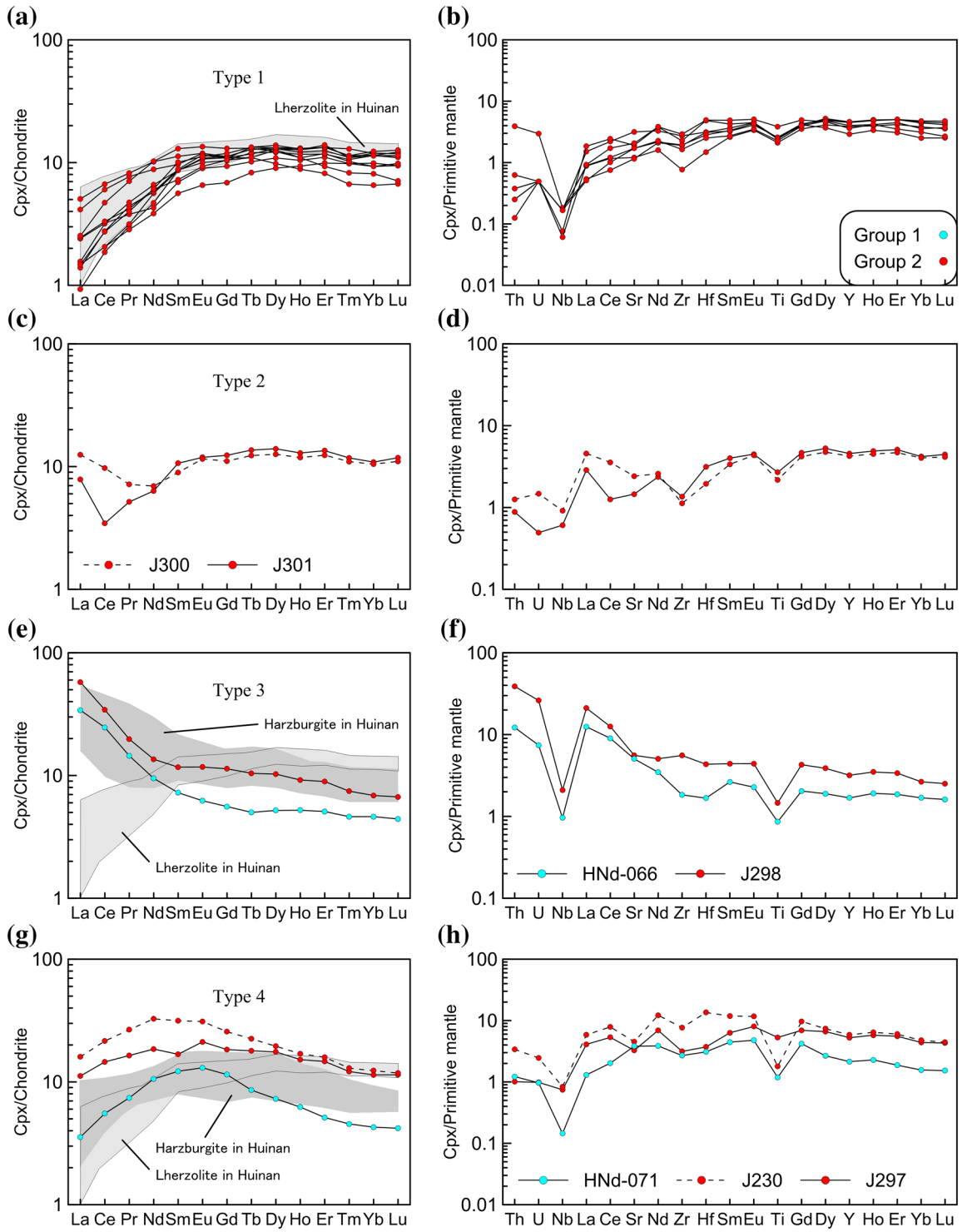

Fig. 6 Chondrite-normalized REE patterns and primitive mantle-normalized trace-element spidergrams for clinopyroxenes from the studied Huinan peridotites. Group 1 peridotites display LREE-enriched (Type 3) and convex-upward (Type 4) REE patterns. Group 2 xenoliths mainly show LREE-depleted (Type 1) and spoon-shaped (Type 2) REE patterns, besides minor Type 3 and Type 4 ones. Chondrite and primitive mantle data are from McDonough and Sun (1995). Lherzolite and Harzburgite in Huinan of grey fields are from Xu et al. (2003b)

Equilibrium temperatures

Equilibration temperatures (T) have been estimated using three thermometers based on: (1) Fe–Mg partitioning between pyroxenes (i.e., $T_{(Wells)}$; Wells 1977); (2) Ca content in orthopyroxene (i.e., $T_{(BK)*}$) following the method of Brey and Köhler (1990) modified by Nimis and Grütter (2010), and (3) enstatite in sole clinopyroxene, which was calibrated for garnet peridotites but can be used to calculate apparent temperatures for spinel peridotites (i.e., $T_{(NT)}$; Nimis and Taylor 2000). Temperature estimates only use the average core compositions of minerals. Due to the lack of reliable geobarometers, all these estimates assume a pressure of 1.5 GPa, a reasonable value for spinel-facies peridotites (e.g., Ziberna et al. 2013), for consistency with peridotite xenoliths from eastern China (Table S5; Xu et al. 1993; Zheng et al. 2007). Most $T_{(Wells)}$ and $T_{(NT)}$ are higher than $T_{(BK)*}$, which can generally be reconciled with the uncertainties of used thermometers (e.g., 70 °C for $T_{(Wells)}$, Wells 1977; 30 °C for $T_{(NT)}$, Nimis and Taylor 2000) and disequilibrium between the pyroxenes. The opx in the studied peridotites has low Na_2O (0.03–0.31 wt.%, mainly 0.07–0.11 wt.%) whereas the cpx has a large Na_2O range (0.36–1.92 wt.%; Table S3), which probably affects T estimates using cpx methods due to Na–Ca substitution (Ionov et al. 2018). Thus, we consider that $T_{(BK)*}$ may be a more reliable estimate. $T_{(BK)*}$ for Group 1 and Group 2 xenoliths studied here is 923–977 °C and 881–1110 °C, respectively. These estimates are in agreement with the temperature range previously reported for peridotites from the Longgang block (880–1197 °C; Wu et al. 2003; Wang et al. 2013).

Discussion

Depletion vs. refertilization of the lithospheric mantle beneath Huinan

Cratonic mantle, mainly composed of peridotites, underwent complex melt extraction (depletion) and metasomatic processes (refertilization) (Zheng 2009; Tang et al. 2013). Therefore, geochemical characteristics of peridotite and its minerals will record the superposition of multiple deep processes and mantle properties at the time of entrainment. Mantle partial melting should lead to the depletion of fusible phases (i.e., cpx and sp) and basaltic components (i.e., SiO_2, Al_2O_3, CaO, TiO_2 and Na_2O) in residues, and the increase of MgO contents and Mg# values (Niu 1997; Herzberg 2004). This would be accompanied by mineralogical changes whereby lherzolite evolves into harzburgite and finally dunite, accompanied by increasing Mg# (Walter 2003). In contrast, refertilization by addition of variable amounts of silicate melts could induce reverse variations (Griffin et al. 2003; Zhang 2009; Tang et al. 2013; Xiong et al. 2015) that are difficult to distinguish from originally undepleted lithosphere. Thus, linear arrays in MgO vs. oxide space can be interpreted by binary mixing between depleted peridotite and a basaltic melt (e.g., Chin et al. 2014). The studied Huinan peridotites have high whole rock MgO contents and low HREE levels of clinopyroxenes (Figs. 3, 6). Moreover, Al_2O_3 and CaO in a few samples of Group 1 follow a partial melting trend (Fig. 4b, d), and the Group 2 peridotites mainly show LREE-depleted patterns (Fig. 6a). Prima facie, these petrochemical features suggest a variably depleted mantle source.

Partial melting trends of primitive mantle modeled according to Herzberg (2004) and Niu (1997) have been used in the literature to constrain the minimum fractions of partial melting (F) and the melting conditions (Fig. 4). The comparison shows that the majority of Group 1 peridotites could have been produced by > 18% fractional melting or batch melting, whereas most of Group 2 xenoliths apparently require < 16% partial melting in a pressure range of 0.5–2.5 GPa (Fig. 4). Melt fractions can be also estimated from the HREE in clinopyroxene at spinel-facies condition (Fig. S1) following the approach of Johnson et al. (1990), or from the Cr# values of spinel (Hellebrand et al. 2001). However, application of these models produces conflicting results: Cpx modeling indicates that Group 1 peridotites experienced 10–12% degrees of partial melting, whereas the Group 2 xenoliths were subjected to low degrees of partial melting (i.e., 0–8%). In contrast, the degrees of partial melting for the Group 1 xenoliths calculated by spinel Cr# are lower than those based on whole-rock compositions, while similar partial melting degrees for the Group 2 peridotites can be obtained by above methods (Table S3).

Nevertheless, it is also obvious in Fig. 4 that only a few Group 1 samples actually plot on expected melt depletion trends, whereas most samples have higher FeO contents and lower Mg# than primitive mantle models at a given Al_2O_3 content (Fig. 4a, b), e.g., sample HNd-083 with Mg# of 87.6, which significantly deviates from the partial melting trend of residual peridotites. Furthermore, whole rock compositions are characterized by impoverishment in SiO_2 compared with the partial melting trends (Fig. 4c). The trend of CaO vs. Al_2O_3 in Huinan peridotites is more characteristic of mixing than of melt depletion (Fig. 4d). In addition, apparently linear correlations between the Mg# and Al_2O_3, Cr_2O_3, TiO_2 and Na_2O contents in pyroxenes of the studied peridotites (Fig. 5c-f) are the combined results of early depletion and subsequent melt infiltration (Zhang et al. 2008; Zhang 2009). Finally, various LREE enrichments of clinopyroxene (Fig. 6) and high TiO_2 contents in spinels, with obvious deviation from the melting trend, suggest reaction between melts and peridotite (Pearce et al. 2000; Xu et al. 2003b; Fig. 7). These observations indicate that the peridotite xenoliths from

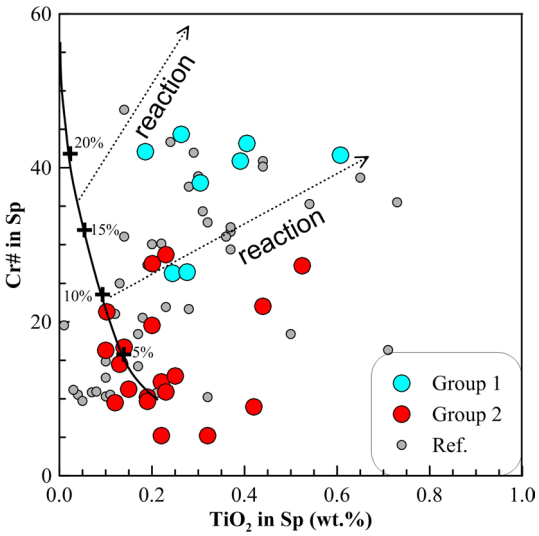

Fig. 7 Cr# versus TiO_2 in spinel for the studied Huinan peridotites. Melting trend and parameters are from Xu et al. (2003b). Data sources are as in Fig. 3

Huinan could have experienced various degrees of depletion and profound refertilization. Refertilization not only affects the major element compositions of whole rocks, but can also introduce spinel and clinopyroxene with elevated HREE and Y concentrations. Thus, we emphasize that the estimates of melt fractions extracted from these samples must be minimum, resulting in low apparent degrees of depletion. That said, combined with a comparison of the major elements in whole rocks (Fig. 3) and minerals (Fig. 5), our results clearly indicate that the Group 1 peridotites are moderately refractory, whereas Group 2 xenoliths are more fertile, which will be further discussed in the following section.

Diverse metasomatic effects on refractory vs. fertile SCLM

Peridotite xenoliths from Huinan show various REE patterns of clinopyroxene (Fig. 6), which cannot be explained solely by melt extraction, but must reflect subsequent modification. Mantle metasomatism may be also evidenced by petrographic features. Although the sieve texture of spinel has been identified as a result of partial melting (Su et al. 2011), the sieve-textured spinels in the studied Huinan xenoliths show Mg# decrease, Fe and Ti contents increase and Cr# increase from the cores to the sieved rims (Table S3). These features are, therefore, more consistent with melt–peridotite interaction (Shaw et al. 2006).

Cryptic and stealth metasomatic overprints

Patent metasomatism is typically evidenced by the presence of hydrous minerals (phlogopite, amphibole) and/or carbonate or other exotic minerals (Dawson 1984), which are not recognized in the xenoliths under study. Conversely, cryptic metasomatism leads to enrichment in incompatible trace elements, whereby clinopyroxene is commonly considered as the major carrier of incompatible trace elements in anhydrous garnet-free peridotites (Bedini and Bodinier 1999; Zangana et al. 1999; Xu et al. 2003a), with the exception of orthopyroxene containing some proportions of lithophile trace elements (e.g., HFSE; Byerly and Lassiter 2015) at high temperatures (Witt-Eickschen and O'Neill 2005). Bearing in mind that the trace-element distribution of some elements between the pyroxenes can be affected by subsolidus re-equilibration, clinopyroxene can, therefore, provide useful information on mantle processes, such as partial melting and metasomatic enrichment (Bodinier et al. 1990; Johnson et al. 1990; Hellebrand et al. 2002; Aulbach et al. 2017b).

The different REE patterns of clinopyroxene represent snapshots of different metasomatic agents and/or diverse metasomatic effects of percolating melts or fluids. In the latter situation, melt percolation can give rise to spatial changes in trace element contents as a result of ion-exchange chromatographic effects controlled by mineral/melt partition coefficients of elements (Ionov et al. 2002; Navon and Stolper 1987). The diffusion rates of elements through the porous peridotites are inversely proportional to their solid-melt partition coefficients, which can lead to enrichment of the highly incompatible elements (e.g., LREE) in the chromatographic front with respect to the moderately incompatible (e.g., HREE) and compatible ones (Xu et al. 2003b). Therefore, an identical initial metasomatic medium can produce a series of trace element signatures over a certain distance. At the same time, the extent of metasomatism (or enrichment) decreases with the increase of the distance between melt and rock (Yu et al. 2005).

In this model, Type 1 clinopyroxenes with LREE-depleted REE patterns are explained as the products of equilibration with LREE-depleted melts (Rivalenti et al. 2007; Rampone et al. 2010; Princivalle et al. 2014) rather than melt residues, consistent with their failure to fall on mantle residue trends (Fig. 4), as discussed in the previous section. The spoon-shaped REE patterns of Type 2 peridotites and the convex-upward REE patterns, with enrichment in LREE and humps in Nd or Eu, of Type 4 peridotites could be due to chromatographic effects related to the same metasomatic melt (e.g., Ionov et al. 2002). Conversely, the HREE and Y depletion in the single group 1 peridotite of this type could be related to an entirely different effect, namely preserved equilibration with garnet that has decomposed to spinel-pyroxene assemblages (Fig. 2a, b). This will be further discussed in a later section. The observed LREE enrichment in Type 3 cpx is difficult to reproduce via interaction between alkaline basalts and LREE-depleted ambient peridotite (Rivalenti

et al. 2007), suggesting that it results from multiple metasomatic events. Indeed, multistage metasomatism has been proposed on the basis of the Li elemental and isotopic compositions of Longgang mantle xenoliths and was attributed to melts/fluids derived from the subducted Pacific plate and the asthenosphere (Tang et al. 2012).

Finally, the afore-described metasomatism not only had cryptic effects, but was likely accompanied by modal changes representing stealth effects (O'Reilly and Griffin 2012). For example, interaction with silica-undersaturated melts, such as alkaline basalts, can lead to precipitation of olivine (and cpx) at the expense of opx (Pearson and Wittig 2014), which is not necessarily evident from the microstructures or modal abundances. Indeed, Xu et al. (2003a, b) argue that the Huinan harzburgites resulted from interaction between peridotites and percolating melts, transforming lherzolite to harzburgite by the preferential dissolution of pyroxenes and precipitation of olivine. While olivine enrichment can explain the low SiO_2 content at a given Al_2O_3 content recorded in most peridotite xenoliths from Huinan (Fig. 4c), this process alone cannot explain why Group 1 harzburgites have consistently higher Mg# than Group 2 lherzolites (Table S1), which is ascribed to melt depletion without strong refertilization.

Metasomatic agents and the effect of mineralogy

As outlined in the introduction, metasomatic agents in the SCLM include, but are not limited to, carbonatitic melts (Ionov et al. 1993; Rudnick et al. 1993), volatile-rich silicate melts (Zangana et al. 1999) and H_2O-CO_2 fluids (Gorring and Kay 2000; Xu et al. 2003a). Compared with silicate melts, carbonatite melts are usually enriched LILE and can fractionate HFSE and REE more efficiently (Blusztajn and Shimizu 1994). Thus, low Ti/Eu ratios, HFSE depletion and high $(La/Yb)_N$ ratios in clinopyroxenes have been widely interpreted as a key signature of carbonatite-related metasomatism (Rudnick et al. 1993; Coltorti et al. 1999). The cpx in the studied Group 2 peridotites have predominantly high Ti/Eu (2331–5947) and low $(La/Yb)_N$ (0.08–7.94) ratios (except J230) and fall in the silicate metasomatism area of the Ti/Eu-$(La/Yb)_N$ diagram (Fig. 8), similar to the fertile peridotites from Shanwang that underwent silicate-melt metasomatism (Zheng et al. 1998). Group 2 sample J230 plots outside both the silicate and the carbonatitic metasomatism area, which may reflect superposition of multiple metasomatism as discussed above. In contrast, two Group 1 samples (J298 and HNd-066), which generally show garnet-breakdown textures, probably still reflect equilibrium with former garnet and their elevated $(La/Yb)_N$ can therefore not be unambiguously ascribed to carbonatitic metasomatism, as discussed in the following section.

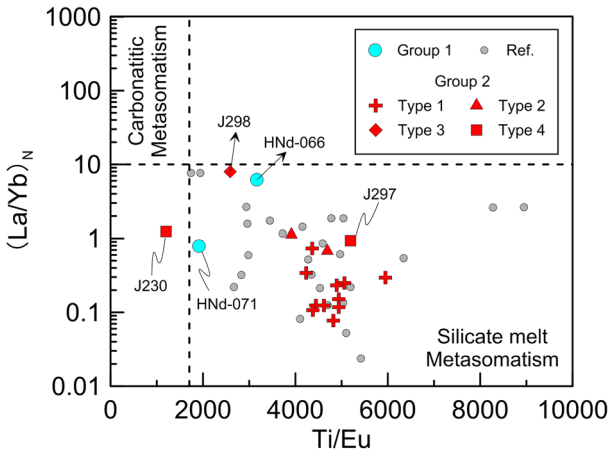

Fig. 8 $(La/Yb)_N$ vs. Ti/Eu of clinopyroxenes from the studied Huinan peridotites; subscript N denotes normalization to chondrite (McDonough and Sun 1995). Modified from Coltorti et al. (1999). Data sources as in Fig. 3

To further constrain the nature of the metasomatic agents, hypothetical liquids in equilibrium with clinopyroxenes were calculated using the cpx/melt partition coefficients listed by Ionov et al. (2002). Some differences between the calculated melt and the host basalts may arise from the effect of temperature on trace element distribution (e.g., Lee et al. 2007), since the partition coefficient used here was determined at temperatures about 1300 °C, much higher than those of the studied peridotites (881 to 1110 °C), which are below the dry peridotite solidus at 1.5GPa (Hirschmann 2000). Calculated melts are largely similar to the alkaline basalts erupted in the Longgang region (Liu et al. 1994; Chen et al. 2007; Yan et al. 2007), except for lower Ta, Ti, La and Ce and higher Nb contents in the calculated melts (Fig. 9a). Differences in the HFSE can be explained by subsolidus redistribution into opx, whereas higher HREE and lower LREE contents may indicate that the metasomatic melt formed by a higher melt fraction than the basalts that entrained the xenoliths (Fig. 9b). However, for sample J230, the contents of most elements of the calculated melts are higher than those of the alkaline basalts (Fig. 9a), possibly due to the influence of multi-stage metasomatic overprints, which is also supported by its position at the low-Ti/Eu extreme in the Ti/Eu-$(La/Yb)_N$ diagram (Fig. 8).

Of note, cpx in the two Group 1 samples and a minority of Group 2 samples have lower Ti/Eu and higher La/Yb. This may reflect chromatographic effects described above, implying a smaller degree of melt–rock interaction at a greater distance from the unreacted melt. Alternatively or additionally, mineralogy may play a role: Refractory peridotites (harzburgites, dunites) have higher solidi than lherzolites, which is permissive of interaction with a fluid or small-volume residual liquid but impedes percolation of

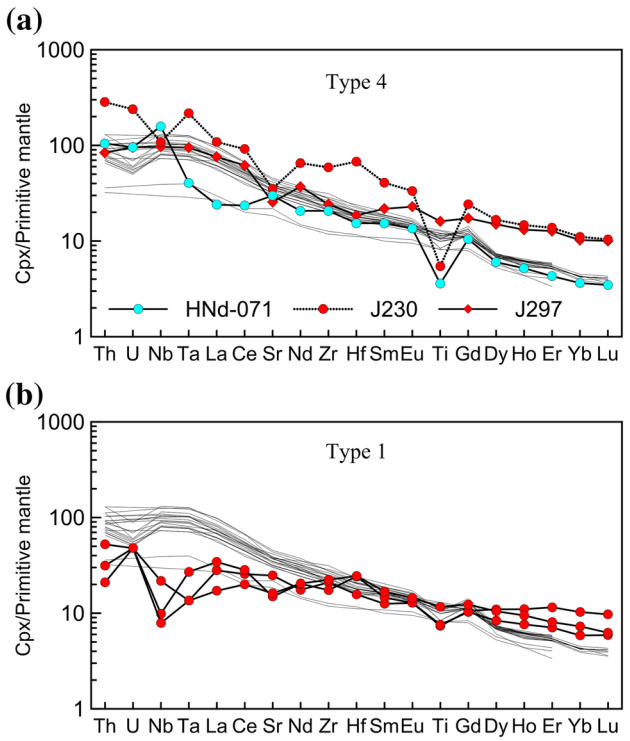

Fig. 9 Calculated compositions of melts in equilibrium with clinopyroxene from: **a** Type 4 samples; **b** selected Type 1 samples. Cpx/melt partition coefficients are from Ionov et al. (2002). The compositions of Cenozoic basalts (Chen et al. 2007; Liu et al. 1994; Yan et al. 2007) of the Huinan region are shown for comparison (gray lines)

volatile-poor silicate melts, whereas lherzolites can be in equilibrium with such melts (Stachel and Luth 2015). In this model, the diverse metasomatic effects by silicate melts on the studied Huinan peridotites can, at least partially, be explained by the difference of fertility in the SCLM.

A refined mechanism for destruction and replacement of the SCLM beneath the eastern NCC

Pseudomorphs after garnet resulting from rifting and decompression

It is conspicuous that Group 1 samples are characterized by spinel–pyroxene intergrowths, which are generally considered to be formed by garnet breakdown reactions during a transition of lithospheric mantle from the garnet stability field to the spinel stability field (Smith 1977; Rampone et al. 2010; Bhanot et al. 2017; Casagli et al. 2017), and which occupy ovoid or curvilinear shapes (Fig. 2a, b). Similar features have been described for peridotite xenoliths from the North Atlantic Craton in Greenland, where they were interpreted as pseudomorphs after garnet that was destabilized during extension (Aulbach et al. 2017b). Garnet destabilization was similarly described for mantle xenoliths from Antarctica and the East African Rift (Foley et al. 2006; Kaeser et al. 2006). Huinan is located near the Tan-Lu fault belts. All the aforementioned localities were affected by rifting and various degrees of lithosphere thinning, providing a commonality with the samples under investigation. Indeed, extension and melt–SCLM interaction have been ascribed to slab rollback of the subducting Paleo-Pacific plate (Tang et al. 2012; Zheng and Dai 2018) and can explain the decompression evidenced by the suggested pseudomorphs after garnet.

Further evidence for the former presence of garnet in Huinan peridotites comes from the low and variable Al_2O_3 contents over a narrow Mg# range in opx from Group 1 peridotites, which may reflect a superposition of their more refractory compositions and of preserved equilibration with garnet (now present as spinel–pyroxene intergrowths). Because these xenoliths experienced significant refertilization by silicate melt—though less intensive and complete than in the Group 2 xenoliths—it seems reasonable to suggest that this metasomatic event catalyzed garnet breakdown. Concomitant reaction of the garnet breakdown products with the infiltrating melt implies that the reaction was not isochemical. Finally, negative slope in the HREE patterns of Group 1 cpx is also suggestive of equilibration with former garnet rather than reflecting metasomatism because these samples are HREE-depleted rather than LREE-enriched relative to Group 2 cpx. This implies that after decompression, these intergrowths did not fully re-equilibrate with the matrix pyroxenes. Original depletion of the refractory Group 1 peridotites in the garnet stability field would not have fractionated Cr from Al as strongly as melting at spinel-facies conditions (Canil 2004). Residues with intense melting in the garnet field would have a relatively low Cr# value of spinel, which can explain the low estimates of melt fractions for Group 1 spinels (Hellebrand and Snow 2003), compared to estimates based on whole-rock composition. By contrast, the similar extent of melting estimated by both methods for Group 2 may indicate that the re-equilibration was facilitated and catalyzed by strong melt–rock reactions, which is consistent with the only rare occurrence of pyroxene–spinel intergrowths in this group. Therefore, these observations indicate that Group 1 and Group 2 peridotites, representing different domains of SCLM, were initially formed in the garnet stability field.

Because the refractory cratonic mantle has a high solidus temperature, it is impenetrable to refertilizing asthenospheric melts, as discussed above. This aided in the preservation of spinel-pyroxene intergrowths in Group 1 peridotites (Fig. 10d, e), which only show evidence for metasomatism by residual melts at low melt–rock ratios. Conversely, Group 2 peridotites represent decompressing fertile mantle, which was open to pervasive melt percolation,

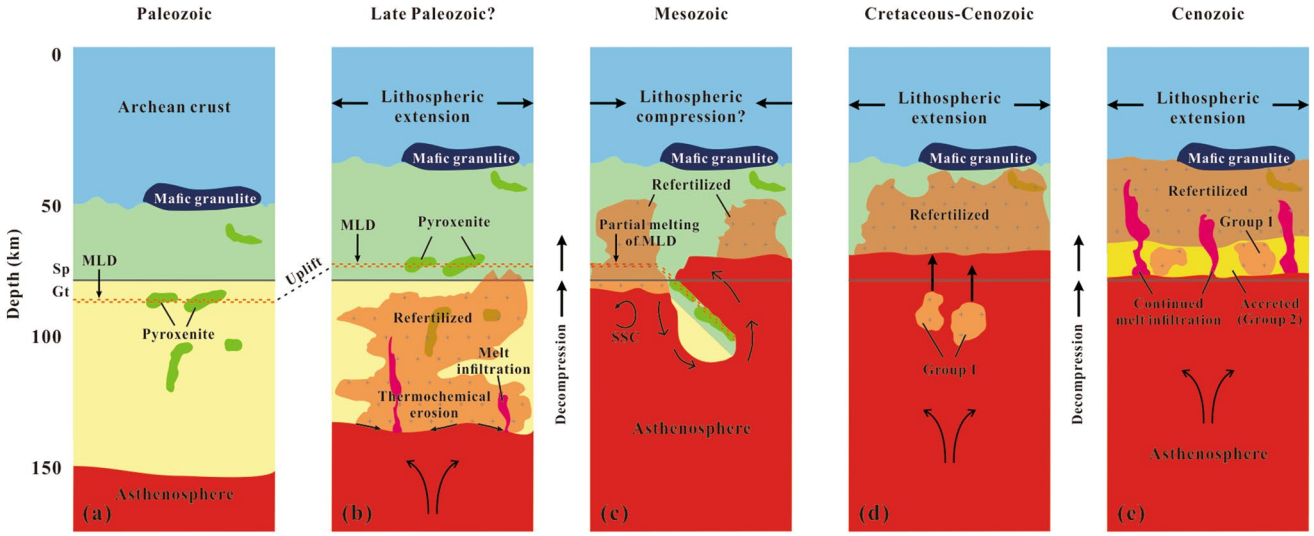

Fig. 10 Schematic illustrating the possible origin of the studied Huinan xenoliths and modification of the SCLM beneath the northeastern NCC. **a** Inferred lithospheric mantle, which consisted of Sp and Gt peridotite and contained an MLD, beneath the Huinan area during Paleozoic time. *Sp* spinel, *Gt* garnet, *MLD* mid-lithospheric discontinuities. **b** Lithospheric extension and uplift, leading to decompression; strong refertilization and densification of the pre-existing ancient lithosphere, which was accompanied by thermochemical erosion, also occurred during asthenospheric upwelling and melt infiltration. **c** Partial melting of MLD due to heating; delamination of parts of the ancient mantle along a pre-existing MLD, possibly in response to multiple subduction events during the Mesozoic, besides small-scale convection (SSC) in the asthenosphere (Liu et al. 2018). **d** Renewed lithospheric extension during the Paleo-Pacific slab retreat led to uplift of asthenosphere, into which the ancient mantle regions had sunk, causing their re-accretion. **e** Both newly accreted material and blebs of relaminated ancient mantle decompressed from garnet stability field; localized melt–rock reaction of both refractory and refertilized overlying mantle portions due to continued melt infiltration, leading to complete destruction of pyroxene–spinel intergrowths after garnet in fertile mantle at high melt–rock ratios, but preservation in refractory harzburgite at low melt–rock ratios (see text for details)

leading to the destruction of pseudomorphs after garnet at high melt–rock ratios (Fig. 10e). We suggest that both lithologies were decompressed from the garnet-stability field, but their different mineralogies and solidi resulted in different styles and intensities of interaction with metasomatic agents, which explains why the spinel–pyroxene intergrowths are rare in the fertile xenoliths, but frequent in the more refractory samples.

Coexistence of two distinct lithospheric mantle sources beneath Huinan

The composition of the SCLM is generally correlated with crustal age and/or tectonic setting (Griffin et al. 1999a). Wu et al. (2003) reported the ages of Longgang peridotite xenoliths suggesting minimum Mesoproterozoic model ages (1.0-–1.2 Ga) for melt depletion of the SCLM, using whole-rock Os isotopes. However, the refertilization processes could mask and even completely obliterate the Archean refractory signatures of parts of the lithosphere, and rejuvenate the Archean mantle by lowering the Re–Os model ages of refertilized peridotites (Tang et al. 2013). In addition, the Longgang Block consists mainly of Neoarchean tonalite–trondhjemite–granodiorite (TTG) rocks (Wan et al. 2005), with only minor occurrences of supracrustalrocks (Anshan Group) that have Sm-Nd isotope model ages of 2800–2500 Ma (Wu et al. 2005b). Recent studies on zircons in high-Mg andesites (Li et al. 2014) and metamorphic rocks from the Seluohe Group (Li et al. 2007) have shown that the Archean basement may be more widespread beneath this region. Therefore, such observations suggest that the age of the SCLM beneath Huinan is likely underestimated, and the SCLM possibly contains—or originally contained—more ancient materials (Fig. 10a).

A comparison of the major elements in whole rocks (Fig. 3) clearly indicates that the Group 1 peridotites are more refractory with an affinity to the refractory mantle beneath Hebi, which represent remnants of the Archean lithosphere preserved locally beneath the NCC (Zheng et al. 2001, 2007). In contrast, Group 2 xenoliths are fertile and similar to those from Shanwang which may represent newly accreted fertile material (Zheng et al. 1998). In terms of texture and degrees of partial melting, Group 1 and Group 2 peridotites are also very similar to the northern and southern SCLM domains beneath the French Massif Central, respectively (Lenoir et al. 2000). So, to some extent, Group 1 and Group 2 peridotites also have an affinity for cratonic and circumcratonic SCLM domains, respectively. The coexistence

of moderately refractory and fertile lithospheric mantle beneath the study area reflects the complex lithospheric architecture and evolution.

The studied Huinan peridotites have various equilibrium temperatures. Assuming equilibration to a single conductive geotherm, in the absence of appropriate geobarometers in spinel-facies peridotites, the different equilibrium temperatures may roughly reflect different source depths. There are no systematic differences in equilibrium temperatures between the two peridotite groups. Given evidence for the former presence of garnet and the fact that Group 1 peridotites are more depleted than the more fertile group 2 peridotites, higher pressures were applied to Group 1 in order to test the effect of pressure, whereas those of Group 2 xenoliths were fixed at 1.5 GPa. This shows that the temperature estimates of Group 1 can be clearly distinguished from Group 2 only when the pressure is above 3.5 GPa, which is deeply in the garnet stability field (Ziberna et al. 2013) (Table S5). However, because garnet was clearly destabilized, probably by depressurization, and because the replacement of the lithosphere beneath the NCC occurred in the Late Cretaceous (Xu 2001), whereas the basalt erupted much later in the Quaternary (Fan et al. 2000), we consider the lower equilibrium temperatures at pressures < 2 GPa to accurately reflect the thermal state of Group 1 peridotites at the time of entrainment (Xu et al. 2003b).

In addition, there is the lack of correlation between Mg# in olivine and equilibrium temperatures (Table S5). These features suggest that the moderately refractory and fertile lithospheric mantle sources are not compositionally stratified but coexist within similar depths intervals, consistent with previous studies (Xu et al. 2003b; Lu and Zheng 2011). The juxtaposition of distinct mantle source regions is quite common in eastern China (Zheng et al. 2007; Lu et al. 2013), and also the eastern Central Asian Orogenic Belt (Pan et al. 2013). Furthermore, the two types of SCLM domains experienced a complex metasomatic process by silicate melts derived from the underlying asthenosphere, but show different metasomatic features, as discussed above (Fig. 6). Collectively, the evidence indicates that the lithospheric mantle beneath the Huinan region is heterogeneous, including fertile Phanerozoic materials and moderately refractory Proterozoic (or even Archean) mantle remnants (Fig. 10e).

Delamination of refractory lithosphere and re-accretion with fertile asthenospheric mantle

Mantle keels are usually stable beneath cratons due to their inherent buoyancy and high viscosity (Griffin et al. 1999a; Wang et al. 2015). However, modification and/or replacement of the SCLM by tectonic processes associated with continental collision, uplifting and magmatism (Griffin et al. 1998, 1999a; Aulbach 2018) can partly or even entirely transform the nature of lithospheric mantle from old, cold, thick and refractory "cratonic" lithospheric mantle to the young, hot, thin and fertile "oceanic" lithospheric mantle (Zheng et al. 1998, 2001, 2007). Refertilization by peridotite–melt reaction is considered a possible mechanism because it can account for the compositional change of the lithospheric mantle and the coexistence of young and old lithospheric mantle (Zhang 2009). Coupled with previous studies, the Sr–Nd–Li isotopic data of the peridotite xenoliths from Huinan provide further evidence that the lithospheric mantle underlying the northeastern NCC experienced multistage interactions between melts/fluids and peridotites (Tang et al. 2012; Xu et al. 2003b).

Combined, the evidence for (1) the former presence of garnet in the inherited refractory peridotites, (2) the coexistence of the latter with fertile mantle over a similar temperature and inferred depth interval, as well as (3) a role of delamination in the destruction of the mantle root beneath the eastern North China Craton based on numerical models (Liu et al. 2018) leads us to propose that portions of ancient lithospheric mantle sank into the convecting mantle after delamination some time after the Mesozoic, followed by re-accretion with fertile mantle during asthensopheric upwelling late Mesozoic-Cenozoic (Fig. 10c–e). These processes of lithosphere delamination and re-accretion were probably related to the closure of the Paleo-Asian Ocean (Xiao et al. 2003; Dai et al. 2018) and the slab rollback of the subducting Paleo-Pacific plate (Tang et al. 2012; Zheng and Dai 2018). During continued upwelling of asthenosphere and extension of the overlying lithosphere, the mixed SCLM (including moderately refractory relics and newly accreted fertile mantle) was diversely metasomatized by silicate melts.

Conclusions

We studied the textures and major and trace element compositions of spinel-facies peridotite xenoliths from the decratonized northeastern part of the North China Craton in order to better understand their petrogenesis and the insights they may provide on the response of the subcontinental lithospheric mantle to the regional complex tectonothermal evolution. Several salient observations lead us to propose a refined model for the destruction and replacement of SCLM beneath the North China Craton:

(1) The samples can be subdivided into two groups: Group 1 peridotites show protogranular textures and represent moderately refractory SCLM (bulk-rock Mg# 90.1–90.7), whereas Group 2 xenoliths display porphyroclastic to protogranular textures and have more fertile mantle composition (bulk-rock Mg# 87.6–90.1).

(2) Clinopyroxenes in the Group 1 xenoliths display LREE-enriched and convex-upward REE patterns, whereas those in Group 2 mainly show LREE-depleted and spoon-shaped REE patterns, with minor LREE-enriched and convex-upward ones. These different metasomatic overprints are ascribed to differences in mineralogy and composition, which results in different solidi and permeability to silicate melts.

(3) The former presence of garnet is supported by low Al_2O_3 contents in some opx and HREE-Y depletion in some cpx and by spinel-pyroxene intergrowths with ovoid shapes apparently occupying former coarse grains. These intergrowths, which suggest decompression from the garnet stability field, are frequent in Group 1, whereas they are rare in Group 2. This difference is again ascribed to the different permeability of fertile vs. refractory peridotite to silicate melts, which catalyze recrystallization and chemical re-equilibration.

(4) Despite these mineralogical and compositional differences, peridotites of both groups have similar equilibration temperatures (i.e., 923–977 °C and 881–1110 °C, respectively), which are not correlated with Mg# in olivines, suggesting that they coexist over a range of depths.

Combined, these observations can be explained if ancient cratonic relics sank into the convecting mantle after delamination and were re-accreted together with more fertile mantle during renewed asthenospheric upwelling and decompression, followed by melt–rock interaction, all of which occurred in response to lithosphere extension caused by rollback of the subducting Pacific plate.

Acknowledgements We thank Editor Othmar Müntener, reviewer Emily J. Chin and an anonymous reviewer for constructive comments and suggestions on the original manuscript. This version benefited from constructive reviews by Emily J. Chin and Qiao Shu, and suggestions and handling by Editor Timothy Grove. This work was supported by the National Natural Science Foundation of China project (41520104003) and the National Key R&D Program of China (2016YFC0600403).

References

Aulbach S (2018) Cratonic Lithosphere discontinuities: dynamics of small-volume melting, meta-cratonisation and a possible role for brines. In: Yuan H, Romanowicz B (eds) Lithospheric discontinuities geophysical monograph 239. American Geophysical Union, Washington, D.C., pp. 177–204

Aulbach S, Massuyeau M, Gaillard F (2017a) Origins of cratonic mantle discontinuities: a view from petrology, geochemistry and thermodynamic models. Lithos 268:364–382. https://doi.org/10.1016/j.lithos.2016.11.004

Aulbach S, Sun J, Tappe S, Höfer HE, Gerdes A (2017b) Volatile-rich metasomatism in the Cratonic Mantle beneath SW Greenland: link to Kimberlites and Mid-lithospheric discontinuities. J Petrol 58:2311–2338. https://doi.org/10.1093/petrology/egy009

Bedini RM, Bodinier JL (1999) Distribution of incompatible trace elements between the constituents of spinel peridotite xenoliths: ICP-MS data from the East African rift. Geochim Cosmochim Acta 63:3883–3900

Bernstein S, Kelemen P, Hanghøj K (2007) Consistent olivine Mg# in cratonic mantle reflects Archean mantle melting to the exhaustion of orthopyroxene. Geology 35:459–462. https://doi.org/10.1130/G23336A.1

Bhanot KK, Downes H, Petrone CM, Humphreys-Williams E (2017) Textures in spinel peridotite mantle xenoliths using micro-CT scanning: examples from Canary Islands and France. Lithos 276:90–102. https://doi.org/10.1016/j.lithos.2016.08.004

Blusztajn J, Shimizu N (1994) The trace-element variations in clinopyroxenes from spinel peridotite xenoliths from southwest Poland. Chem Geol 111:227–243

Bodinier JL, Vasseur G, Vernieres J, Dupuy C, Fabries J (1990) Mechanisms of mantle metasomatism: geochemical evidence from the Lherz orogenic peridotite. J Petrol 31:597–628

Brey GP, Köhler T (1990) Geothermobarometry in four-phase lherzolites II. New thermobarometers, and practical assessment of existing thermobarometers. J Petrol 31:1353–1378

Byerly BL, Lassiter JC (2015) Trace element partitioning and Lu-Hf isotope systematics in spinel peridotites from the Rio Grande Rift and Colorado Plateau: towards improved age assessment of clinopyroxene Lu/Hf-$^{176}Hf/^{177}Hf$ in SCLM peridotite. Chem Geol 413:146–158. https://doi.org/10.1016/j.chemgeo.2015.08.009

Canil D (2004) Mildly incompatible elements in peridotites and the origins of mantle lithosphere. Lithos 77:375–393. https://doi.org/10.1016/j.lithos.2004.04.014

Casagli A, Frezzotti ML, Peccerillo A, Tiepolo M, De Astis G (2017) (Garnet)-spinel peridotite xenoliths from Mega (Ethiopia): evidence for rejuvenation and dynamic thinning of the lithosphere beneath the southern Main Ethiopian Rift. Chem Geol 455:231–248. https://doi.org/10.1016/j.chemgeo.2016.11.001

Chen Y, Zhang YX, Graham D, Su SG, Deng JF (2007) Geochemistry of Cenozoic basalts and mantle xenoliths in Northeast China. Lithos 96:108–126. https://doi.org/10.1016/j.lithos.2006.09.015

Chen L, Jiang MM, Yang JH, Wei ZG, Liu CZ, Ling Y (2014) Presence of an intralithospheric discontinuity in the central and western north China Craton: implications for destruction of the craton. Geology 42:223–226. https://doi.org/10.1130/G35010.1

Chin EJ, Lee CTA, Barnes J (2014) Thickening, refertilization, and the deep lithosphere filter in continental arcs: constraints from major and trace elements and oxygen isotopes. Earth Planet Sci Lett 397:184–200. https://doi.org/10.1016/j.epsl.2014.04.022

Coltorti M, Bonadiman C, Hinton RW, Siena F, Upton BGJ (1999) Carbonatite metasomatism of the oceanic upper mantle: evidence from clinopyroxenes and glasses in ultramafic xenoliths of Grande Comore, Indian Ocean. J Petrol 40:133–165

Dai HK, Zheng JP, Xiong Q, Su YP, Pan SK, Ping XQ, Zhou X (2018) Fertile lithospheric mantle underlying ancient continental crust beneath the northwestern north China craton: significant effect from the southward subduction of the Paleo–Asian Ocean. Geol Soc Am Bull 131:3–20. https://doi.org/10.1130/B31871.1

Dawson JB (1984) Contrasting types of upper mantle metasomatism? In: Kornprobst J (ed) Kimberlites II. The mantle and crust-mantle relationships. Elsevier, Amsterdam, pp 289–294

Fan QC, Sui JL, Liu RX, Wei HQ, Li N (2000) Petrology and geochemistry of Jinlongdingzi active volcano—the most recent basaltic explosive volcano at Longgang. Chin J Geochem 19:312–317

Fan QC, Sui JL, Liu RX, Wei HQ, Li DM, Sun Q, Li N (2002) Periods of quarternary volcanic activity in Longgang area, Jilin province. Acta Petrol Sin 18:495–500 (**In Chinese with English abstract**)

Foley SF (2008) Rejuvenation and erosion of the cratonic lithosphere. Nat Geosci 1:503–510. https://doi.org/10.1038/ngeo261

Foley SF, Andronikov AV, Jacob DE, Melzer S (2006) Evidence from Antarctic mantle peridotite xenoliths for changes in mineralogy, geochemistry and geothermal gradients beneath a developing rift. Geochim Cosmochim Acta 70:3096–3120. https://doi.org/10.1016/j.gca.2006.03.010

Frey FA, Green DH (1974) The mineralogy, geochemistry and origin of lherzolite inclusions in Victorian basanites. Geochim Cosmochim Acta 38:1023–1059

Gao S, Rudnick RL, Carlson RW, McDonough WF, Liu YS (2002) Re–Os evidence for replacement of ancient mantle lithosphere beneath the North China craton. Earth Planet Sci Lett 198:307–322

Gao S, Rudnick RL, Yuan HL, Liu XM, Liu YS, Xu WL, Ling WL, Ayers J, Wang XC, Wang QH (2004) Recycling lower continental crust in the North China craton. Nature 432:892–899

Gorring ML, Kay SM (2000) Carbonatite metasomatized peridotite xenoliths from southern Patagonia: implications for lithospheric processes and Neogene plateau magmatism. Contrib Mineral Petrol 140:55–72

Griffin WL, O'Reilly SY, Ryan CG, Gaul O, Ionov DI (1998) Secular variation in the composition of subcontinental lithospheric mantle: geophysical and geodynamic implications. In: Braun J, Dooley JC, Goleby BR, van der Hilst RD, Klootwijk CT (eds) Structure and evolution of the Australian continent. Geodynamics, vol 26. American Geophysical Union, Washington, pp 1–26

Griffin WL, O'Reilly SY, Ryan CG (1999a) The composition and origin of subcontinental lithospheric mantle. In: Fei Y, Berka CM, Mysen BO (eds) Mantle petrology: field observations and high-pressure experimentation, pp 13–45

Griffin WL, Ryan CG, Kaminsky FV, O'Reilly SY, Natapov LM, Win TT, Kinny PD, Ilupin IP (1999b) The Siberian lithosphere traverse: mantle terranes and the assembly of the Siberian Craton. Tectonophysics 310:1–35

Griffin WL, O'Reilly SY, Abe N, Aulbach S, Davies RM, Pearson NJ, Doyle BJ, Kivi K (2003) The origin and evolution of Archean lithospheric mantle. Precambrian Res 127:19–41. https://doi.org/10.1016/S0301-9268(03)00180-3

Hellebrand E, Snow JE (2003) Deep melting and sodic metasomatism underneath the highly oblique-spreading Lena Trough (Arctic Ocean). Earth Planet Sci Lett 216:283–299. https://doi.org/10.1016/S0012-821X(03)00508-9

Hellebrand E, Snow JE, Dick HJB, Hofmann AW (2001) Coupled major and trace elements as indicators of the extent of melting in mid-ocean-ridge peridotites. Nature 410:677–681

Hellebrand E, Snow JE, Hoppe P, Hofmann AW (2002) Garnet-field melting and late-stage refertilization in 'residual' abyssal peridotites from the Central Indian Ridge. J Petrol 43:2305–2338

Herzberg C (2004) Partial crystallization of mid-ocean ridge basalts in the crust and mantle. J Petrol 45:2389–2405. https://doi.org/10.1093/petrology/egh040

Hirschmann MM (2000) Mantle solidus: experimental constraints and the effects of peridotite composition. Geochem Geophys Geosyst 1:2000GC000070

Hu ZC, Gao S, Liu YS, Hu SH, Chen HH, Yuan HL (2008) Signal enhancement in laser ablation ICP-MS by addition of nitrogen in the central channel gas. J Anal At Spectrom 23:1093–1101. https://doi.org/10.1039/B804760J

Ionov DA, Dupuy C, O'Reilly SY, Kopylova MG, Genshaft YS (1993) Carbonated peridotite xenoliths from Spitsbergen: implications for trace element signature of mantle carbonate metasomatism. Earth Planet Sci Lett 119:283–297

Ionov DA, Bodinier JL, Mukasa SB, Zanetti A (2002) Mechanisms and sources of mantle metasomatism: major and trace element compositions of peridotite xenoliths from Spitsbergen in the context of numerical modelling. J Petrol 43:2219–2259

Ionov DA, Doucet LS, Xu YG, Golovin AV, Oleinikov OB (2018) Reworking of Archean mantle in the NE Siberian craton by carbonatite and silicate melt metasomatism: evidence from a carbonate-bearing, dunite-to-websterite xenolith suite from the Obnazhennaya kimberlite. Geochim Cosmochim Acta 224:132–153. https://doi.org/10.1016/j.gca.2017.12.028

Johnson KTM, Dick HJB, Shimizu N (1990) Melting in the oceanic upper mantle: an ion microprobe study of diopsides in abyssal peridotites. J Geophys Res 95:2661–2678

Kaeser B, Kalt A, Pettke T (2006) Evolution of the lithospheric mantle beneath the Marsabit volcanic field (northern Kenya): constraints from microstructural, P–T and geochemical studies on xenoliths. J Petrol 47:2149–2184. https://doi.org/10.1093/petrology/egl040

Lee C-T, Harbert A, Leeman WP (2007) Extension of lattice strain theory to mineral/mineral rare-earth element partitioning: an approach for assessing disequilibrium and developing internally consistent partition coefficients between olivine, orthopyroxene, clinopyroxene and basaltic melt. Geochim Cosmochim Acta 71:481–496. https://doi.org/10.1016/j.gca.2006.09.014

Lee C-TA, Luffi P, Chin EJ (2011) Building and destroying continental mantle. Annu Rev Earth Planet Sci 39:59–90. https://doi.org/10.1146/annurev-earth-040610-133505

Lenoir X, Garrido CJ, Bodinier JL, Dautria JM (2000) Contrasting lithospheric mantle domains beneath the Massif Central (France) revealed by geochemistry of peridotite xenoliths. Earth Planet Sci Lett 181:359–375

Li CD, Zhang FQ, Miao LC, Xie HQ, Hua YQ, Xu YW (2007) Reconsideration of the Seluohe Group in Seluohe Area, Jilin Province. J Jilin Univ (Earth Sci) 37:841–847 (**In Chinese with English abstract**)

Li CD, Xu YW, Zhang QH, Zhou HY, Peng SH, Chen JQ, Zhang K, Zhao LG, Li SY (2014) Neoarchean high-Mg andesites and its geological significance in Southern Jilin Province. J Jilin Univ (Earth Sci) 44:186–197 (**In Chinese with English abstract**)

Lin J, Liu YS, Yang YH, Hu ZC (2016) Calibration and correction of LA-ICP-MS and LA-MC-ICP-MS analyses for element contents and isotopic ratios. Solid Earth Sci 1:5–27. https://doi.org/10.1016/j.sesci.2016.04.002

Liu JQ (1999) Volcanoes in China. Science Press of China, Beijing, p 219 (**In Chinese**)

Liu RX, Chen WJ, Sun JZ, Li DM (1992) The K–Ar age and tectonic environment of Cenozoic volcanic rock in China. In: Liu RX (ed) The age and geochemistry of Cenozoic volcanic rock in China. Seismologic Press, Beijing, pp 1–43 (**In Chinese**)

Liu CQ, Masuda A, Xie GH (1994) Major-and trace-element compositions of Cenozoic basalts in eastern China: petrogenesis and mantle source. Chem Geol 114:19–42

Liu YS, Hu ZC, Gao S, Günther D, Xu J, Gao CG, Chen HH (2008) In situ analysis of major and trace elements of anhydrous minerals by LA-ICP-MS without applying an internal standard. Chem Geol 257:34–43. https://doi.org/10.1016/j.chemgeo.2008.08.004

Liu L, Morgan JP, Xu YG, Menzies M (2018) Craton destruction part I: cratonic keel delamination along a weak Mid-Lithospheric discontinuity layer. J Geophys Res 123:10,040–010,068. https://doi.org/10.1029/2017JB015372

Lu JG, Zheng JP (2011) Mineralogical chemistry of peridotite xenoliths from the Huinan Cenozoic basalts: implication for evolution of the lithospheric mantle beneath the North China Craton. Acta Geol Sin 85:330–342 (**In Chinese with English abstract**)

Lu JG, Zheng JP, Griffin WL, Yu CM (2013) Petrology and geochemistry of peridotite xenoliths from the Lianshan region: Nature and evolution of lithospheric mantle beneath the lower Yangtze block. Gondwana Res 23:161–175. https://doi.org/10.1016/j.gr.2012.01.008

McDonough WF, Sun SS (1995) The composition of the Earth. Chem Geol 120:223–253

Menzies MA, Fan WM, Zhang M (1993) Palaeozoic and Cenozoic lithoprobes and the loss of> 120 km of Archaean lithosphere, Sino-Korean craton, China. In: Prichard HM, Alabaster T, Harris NBW, Neary CR (eds) Magmatic processes and plate tectonics. Geol Soc, London, vol 76, pp 71–81

Navon O, Stolper E (1987) Geochemical consequences of melt percolation: the upper mantle as a chromatographic column. J Geol 95:285–307

Nimis P, Grütter H (2010) Internally consistent geothermometers for garnet peridotites and pyroxenites. Contrib Miner Petrol 159:411–427. https://doi.org/10.1007/s00410-009-0455-9

Nimis P, Taylor WR (2000) Single clinopyroxene thermobarometry for garnet peridotites. Part I. Calibration and testing of a Cr-in-Cpx barometer and an enstatite-in-Cpx thermometer. Contrib Miner Petrol 139:541–554

Niu YL (1997) Mantle melting and melt extraction processes beneath ocean ridges: evidence from abyssal peridotites. J Petrol 38:1047–1074

O'Reilly SY, Griffin WL (2012) Mantle metasomatism. In: Harlov DE, Austrheim H (eds) Metasomatism and the chemical transformation of rock: lecture notes in earth system sciences. Springer, Berlin, pp 467–528. https://doi.org/10.1007/978-3-642-28394-9_12

O'Reilly SY, Griffin WL, Poudjom YH, Morgan P (2001) Are lithosphere forever? Tracking changes in subcontinental lithospheric mantle through time. GSA Today 11:4–10

Pan SK, Zheng JP, Chu LL, Griffin WL (2013) Coexistence of the moderately refractory and fertile mantle beneath the eastern Central Asian Orogenic Belt. Gondwana Res 23:176–189. https://doi.org/10.1016/j.gr.2012.03.001

Pearce JA, Barker PF, Edwards SJ, Parkinson IJ, Leat PT (2000) Geochemistry and tectonic significance of peridotites from the South Sandwich arc–basin system, South Atlantic. Contrib Miner Petrol 139:36–53

Pearson DG, Wittig N (2014) The formation and evolution of cratonic mantle lithosphere: evidence from mantle xenoliths. In: Holland HD, Turekian KK (eds) Treatise on geochemistry, 2nd edn. Elsevier, Oxford, pp 255–292

Princivalle F, De Min A, Lenaz D, Scarbolo M, Zanetti A (2014) Ultramafic xenoliths from Damaping (Hannuoba region, NE-China): petrogenetic implications from crystal chemistry of pyroxenes, olivine and Cr-spinel and trace element content of clinopyroxene. Lithos 188:3–14. https://doi.org/10.1016/j.lithos.2013.10.013

Rampone E, Vissers RLM, Poggio M, Scambelluri M, Zanetti A (2010) Melt migration and intrusion during exhumation of the Alboran lithosphere: the Tallante mantle xenolith record (Betic Cordillera, SE Spain). J Petrol 51:295–325. https://doi.org/10.1093/petrology/egp061

Rivalenti G, Zanetti A, Girardi VA, Mazzucchelli M, Tassinari CC, Bertotto GW (2007) The effect of the Fernando de Noronha plume on the mantle lithosphere in north-eastern Brazil. Lithos 94:111–131

Rudnick RL, McDonough WF, Chappell BW (1993) Carbonatite metasomatism in the northern Tanzanian mantle: petrographic and geochemical characteristics. Earth Planet Sci Lett 114:463–475

Shaw CS, Heidelbach F, Dingwell DB (2006) The origin of reaction textures in mantle peridotite xenoliths from Sal Island, Cape Verde: the case for "metasomatism" by the host lava. Contrib Mineral Petrol 151:681–697. https://doi.org/10.1007/s00410-006-0087-2

Smith D (1977) The origin and interpretation of spinel-pyroxene clusters in peridotite. J Geol 85:476–482

Stachel T, Luth RW (2015) Diamond formation—where, when and how? Lithos 220:200–220. https://doi.org/10.1016/j.lithos.2015.01.028

Su BX, Zhang HF, Sakyi PA, Yang YH, Ying JF, Tang YJ, Qin KZ, Xiao Y, Zhao XM, Mao Q, Ma YG (2011) The origin of spongy texture in minerals of mantle xenoliths from the Western Qinling, central China. Contrib Mineral Petrol 161:465–482. https://doi.org/10.1007/s00410-010-0543-x

Sun WD, Ding X, Hu YH, Li XH (2007) The golden transformation of the Cretaceous plate subduction in the west Pacific. Earth Planet Sci Lett 262:533–542. https://doi.org/10.1016/j.epsl.2007.08.021

Takazawa E, Frey FA, Shimizu N, Obata M (2000) Whole rock compositional variations in an upper mantle peridotite (Horoman, Hokkaido, Japan): are they consistent with a partial melting process? Geochim Cosmochim Acta 64:695–716

Tang YJ, Zhang HF, Deloule E, Su BX, Ying JF, Xiao Y, Hu Y (2012) Slab-derived lithium isotopic signatures in mantle xenoliths from northeastern North China Craton. Lithos 149:79–90. https://doi.org/10.1016/j.lithos.2011.12.001

Tang YJ, Zhang HF, Ying JF, Su BX (2013) Widespread refertilization of cratonic and circum-cratonic lithospheric mantle. Earth-Sci Rev 118:45–68. https://doi.org/10.1016/j.earscirev.2013.01.004

Vernières JG, Godard M, Bodinier JL (1997) A plate model for the simulation of trace element fractionation during partial melting and magma transport in the Earth's upper mantle. J Geophys Res 102:24771–24784

Walter MJ (1998) Melting of garnet peridotite and the origin of komatiite and depleted lithosphere. J Petrol 39:29–60

Walter MJ (2003) Melt extraction and compositional variability in mantle lithosphere. In: Carlson RW (ed) Treatise on geochemistry. The mantle and core, vol 2. Elsevier, Amsterdam, pp 363–394

Wan YS, Song B, Yang C, Liu DY (2005) Zircon SHRIMP U-Pb geochronology of Archaean rocks from the Fushun-Qingyuan area, Liaoning Province and its geological significance. Acta Geol Sin 79:78–87 (**In Chinese with English abstract**)

Wang T, Zheng Y, Zhang J, Zeng L, Donskaya T, Guo L, Li J (2011) Pattern and kinematic polarity of late Mesozoic extension in continental NE Asia: perspectives from metamorphic core complexes. Tectonics 30. https://doi.org/10.1029/2011TC002896

Wang J, Hattori K, Xie ZP (2013) Oxidation state of lithospheric mantle along the northeastern margin of the North China Craton: implications for geodynamic processes. Int Geol Rev 55:1418–1444. https://doi.org/10.1080/00206814.2013.780722

Wang HL, van Hunen J, Pearson DG (2015) The thinning of subcontinental lithosphere: the roles of plume impact and metasomatic weakening. Geochem Geophys Geosyst 16:1156–1171. https://doi.org/10.1002/2015GC005784

Wells PRA (1977) Pyroxene thermometry in simple and complex systems. Contrib Mineral Petrol 62:129–139

Windley BF, Maruyama S, Xiao WJ (2010) Delamination/thinning of sub-continental lithospheric mantle under eastern China: the role of water and multiple subduction. Am J Sci 310:1250–1293. https://doi.org/10.2475/10.2010.03

Witt-Eickschen G, O'Neill HSC (2005) The effect of temperature on the equilibrium distribution of trace elements between clinopyroxene, orthopyroxene, olivine and spinel in upper mantle peridotite. Chem Geol 221:65–101. https://doi.org/10.1016/j.chemgeo.2005.04.005

Wu FY, Walker RJ, Ren XW, Sun DY, Zhou XH (2003) Osmium isotopic constraints on the age of lithospheric mantle beneath northeastern China. Chem Geol 196:107–129. https://doi.org/10.1016/S0009-2541(02)00409-6

Wu FY, Lin JQ, Wilde SA, Zhang XO, Yang JH (2005a) Nature and significance of the Early Cretaceous giant igneous event in eastern China. Earth Planet Sci Lett 233:103–119. https://doi.org/10.1016/j.epsl.2005.02.019

Wu FY, Zhao GC, Wilde SA, Sun DY (2005b) Nd isotopic constraints on crustal formation in the North China Craton. J Asian Earth Sci 24:523–545. https://doi.org/10.1016/j.jseaes.2003.10.011

Xiao WJ, Windley BF, Hao J, Zhai MG (2003) Accretion leading to collision and the Permian Solonker suture, Inner Mongolia, China: Termination of the central Asian orogenic belt. Tectonics 22:8–21. https://doi.org/10.1029/2002TC001484

Xiong Q, Griffin WL, Zheng JP, O'Reilly SY, Pearson NJ (2015) Episodic refertilization and metasomatism of Archean mantle: evidence from an orogenic peridotite in North Qaidam (NE Tibet, China). Contrib Miner Petrol 169:31. https://doi.org/10.1007/s00410-015-1126-7

Xu YG (2001) Thermo-tectonic destruction of the Archean lithospheric keel beneath the Sino-Korean Craton in China: evidence, timing and mechanism. Phys Chem Earth (A) 26:747–757

Xu YG, Ross JV, Mercier JCC (1993) The upper mantle beneath the Tanlu fault, eastern China: evidence for intra-lithospheric shear zones. Tectonophysics 225:337–360

Xu S, Nagao K, Uto K, Wakita H, Nakai S, Liu CQ (1998) He, Sr and Nd isotopes of mantle-derived xenoliths in volcanic rocks of NE China. J Asian Earth Sci 16:547–556

Xu XS, O'Reilly SY, Griffin WL, Zhou XM (2003a) Enrichment of upper mantle peridotite: petrological, trace element and isotopic evidence in xenoliths from SE China. Chem Geol 198:163–188. https://doi.org/10.1016/S0009-2541(03)00004-4

Xu YG, Menzies MA, Thirlwall MF, Huang XL, Liu Y, Gen XM (2003b) "Reactive" harzburgites from Huinan, NE China: products of the lithosphere-asthenosphere interaction during lithospheric thinning? Geochim Cosmochim Acta 67:487–505

Xu YG, Zhang HH, Qiu HN, Ge WC, Wu FY (2012) Oceanic crust components in continental basalts from Shuangliao, Northeast China: derived from the mantle transition zone? Chem Geol 328:168–184. https://doi.org/10.1016/j.chemgeo.2012.01.027

Yan J, Zhao JX, Liu HQ (2007) Quaternary basalts from Longgang in the north China Craton: petrologenesis and characteristics of the mantle source. Acta Petrol Sin 23:1413–1422 (**In Chinese with English abstract**)

Yu JH, O'Reilly SY, Zhang M, Griffin WL, Xu XS (2005) Roles of melting and metasomatism in the formation of the Lithospheric Mantle beneath the Leizhou Peninsula, South China. J Petrol 47:355–383. https://doi.org/10.1093/petrology/egi078

Zangana NA, Downes H, Thirlwall MF, Marriner GF, Bea F (1999) Geochemical variation in peridotite xenoliths and their constituent clinopyroxenes from Ray Pic (French Massif Central): implications for the composition of the shallow lithospheric mantle. Chem Geol 153:11–35

Zhai MG, Santosh M (2011) The early Precambrian odyssey of the north China Craton: a synoptic overview. Gondwana Res 20:6–25. https://doi.org/10.1016/j.gr.2011.02.005

Zhang HF (2009) Peridotite-melt interaction: a key point for the destruction of cratonic lithospheric mantle. Chin Sci Bull 54:3417–3437

Zhang HF, Yang YH (2007) Emplacement age and Sr-Nd-Hf isotopic characteristics of the diamondiferous kimberlites from the eastern North China Craton. Acta Petrol Sin 23:285–294 (**In Chinese with English abstract**)

Zhang HF, Goldstein SL, Zhou XH, Sun M, Zheng JP, Cai Y (2008) Evolution of subcontinental lithospheric mantle beneath eastern China: Re-Os isotopic evidence from mantle xenoliths in Paleozoic kimberlites and Mesozoic basalts. Contrib Mineral Petrol 155:271–293. https://doi.org/10.1007/s00410-007-0241-5

Zhang SH, Zhao Y, Davis GA, Ye H, Wu F (2014) Temporal and spatial variations of Mesozoic magmatism and deformation in the North China Craton: implications for lithospheric thinning and decratonization. Earth-Sci Rev 131:49–87. https://doi.org/10.1016/j.earscirev.2013.12.004

Zhao GC, Cawood PA, Wilde SA, Sun M, Lu LZ (2000) Metamorphism of basement rocks in the Central Zone of the North China Craton: implications for Paleoproterozoic tectonic evolution. Precambrian Res 103:55–88

Zhao GC, Sun M, Wilde SA, Li SZ (2005) Late Archean to Paleoproterozoic evolution of the North China Craton: key issues revisited. Precambrian Res 136:177–202. https://doi.org/10.1016/j.precamres.2004.10.002

Zheng JP (1999) Mesozoic-Cenozoic mantle replacement and lithospheric thinning, East China. China University of Geosciences Press, Wuhan, p 126 (**In Chinese**)

Zheng JP (2009) Comparison of mantle derived materials from different spatiotemporal settings: implications for destructive and accretional processes of the North China Craton. Chin Sci Bull 54:3397–3416

Zheng JP, Dai HK (2018) Subduction and retreating of the western Pacific plate resulted in lithospheric mantle replacement and coupled basin-mountain respond in the North China Craton. Sci China Earth Sci 61:406–424. https://doi.org/10.1007/s11430-017-9166-8

Zheng JP, O'Reilly SY, Griffin WL, Lu FX, Zhang M (1998) Nature and evolution of Cenozoic lithospheric mantle beneath Shandong peninsula, Sino-Korean craton, eastern China. Int Geol Rev 40:471–499

Zheng JP, O'Reilly SY, Griffin WL, Lu FX, Zhang M, Pearson NJ (2001) Relict refractory mantle beneath the eastern North China block: significance for lithosphere evolution. Lithos 57:43–66

Zheng JP, Griffin WL, O'Reilly SY, Yu CM, Zhang HF, Pearson N, Zhang M (2007) Mechanism and timing of lithospheric modification and replacement beneath the eastern north China Craton: peridotitic xenoliths from the 100 Ma Fuxin basalts and a regional synthesis. Geochim Cosmochim Acta 71:5203–5225. https://doi.org/10.1016/j.gca.2007.07.028

Zhu RX, Yang JH, Wu FY (2012) Timing of destruction of the North China Craton. Lithos 149:51–60. https://doi.org/10.1016/j.lithos.2012.05.013

Ziberna L, Klemme S, Nimis P (2013) Garnet and spinel in fertile and depleted mantle: insights from thermodynamic modelling. Contrib Mineral Petrol 166:411–421. https://doi.org/10.1007/s00410-013-0882-5